A Model-Independent Algorithm to Derive Ca²⁺ Fluxes Underlying Local Cytosolic Ca²⁺ Transients

Alejandra C. Ventura,* Luciana Bruno,* Angelo Demuro,[†] Ian Parker,[†] and Silvina Ponce Dawson*[‡]

*Departamento de Física, Facultad de Ciencias Exactas y Naturales, Universidad de Buenos Aires, Buenos Aires, Argentina; [†]Department of Neurobiology and Behavior, University of California, Irvine, California; and [‡]T10-Theoretical Biology and Biophysics Group, Los Alamos National Laboratory, Los Alamos, New Mexico

ABSTRACT   Local intracellular Ca²⁺ signals result from Ca²⁺ flux into the cytosol through individual channels or clusters of channels. To gain a mechanistic understanding of these events we need to know the magnitude and spatial distribution of the underlying Ca²⁺ flux. However, this is difficult to infer from fluorescence Ca²⁺ images because the distribution of Ca²⁺-bound dye is affected by poorly characterized processes including diffusion of Ca²⁺ ions, their binding to mobile and immobile buffers, and sequestration by Ca²⁺ pumps. Several methods have previously been proposed to derive Ca²⁺ flux from fluorescence images, but all require explicit knowledge or assumptions regarding these processes. We now present a novel algorithm that requires few assumptions and is largely model-independent. By testing the algorithm with both numerically generated image data and experimental images of sparklets resulting from Ca²⁺ flux through individual voltage-gated channels, we show that it satisfactorily reconstructs the magnitude and time course of the underlying Ca²⁺ currents.

INTRODUCTION

The liberation of Ca²⁺ ions from intracellular stores into the cytosol is used as a signaling mechanism by virtually all cell types to regulate different functions. Recent advances in imaging techniques—including enhanced fluorescent Ca²⁺ indicators and confocal imaging systems with improved temporal (1 ms) and spatial (~0.5 μm) resolution (Pawley, 1995)—provide a powerful tool to study these signals. They have revealed the existence of a wide range of events involving the release from single channels, clusters of channels, and global waves (Cheng et al., 1993; Yao et al., 1995). A complete description of these signals requires a detailed knowledge of the magnitude and kinetics of the underlying Ca²⁺ flux or current. These cannot readily be inferred from fluorescence Ca²⁺ images. In the first place, the images reflect Ca²⁺ ions bound to the fluorescent indicator. Secondly, but more difficult to solve, Ca²⁺ ions do not diffuse freely upon release: endogenous buffers and pumps affect their spatiotemporal dynamics in ways that are hard to determine.

Various methods for estimating Ca²⁺ release fluxes have been presented in the literature, especially in the case of *sparks* in cardiac, skeletal, and smooth muscle. As described in Rios and Brum (2002), they can be classified in two categories:

1. *Forward* calculations, in which a model of intracellular Ca²⁺ dynamics is numerically simulated, and the fluorescent image that such a model produces is compared to the experimental observation (see, e.g., Smith et al., 1998; Baylor et al., 2002; Izu et al., 2001).

2. *Backward* calculations, in which, starting from a given image, the underlying Ca²⁺ current is computed (see, e.g., Blatter et al., 1997; Rios et al., 1999; Rios and Brum, 2002; Soeller and Cannell, 2002).

Regardless of the approach, all of these methods require a working model of cytosolic Ca²⁺ dynamics. Moreover, quantitative data including the kinetics and concentrations of endogenous buffers and pumps are needed (Smith et al., 1998; Izu et al., 2001; Rios and Brum, 2002; Soeller and Cannell, 2002; Blatter et al., 1997; Lukyanenko et al., 1998; Rios et al., 1999), and have been obtained either from experimental studies or by adjustment of parameters within the model to provide the best agreement with the observations (Blatter et al., 1997; Timmer et al., 1998). In most cell types, however, knowledge of their intracellular Ca²⁺ buffers is much less complete than in well-characterized muscle cells, so that these approaches are not generally applicable.

We propose here a novel, model-independent algorithm to obtain Ca²⁺ release fluxes from intracellular fluorescence images, which is particularly suitable for images obtained by optical single ion channel experiments. The method is applicable when Ca²⁺ release is clearly localized in space and time. It only needs a priori information on the kinetics and diffusion parameters of the dye and relies on geometric assumptions that allow us to extrapolate line-scan information into information on the whole space. It does not need, however, any a priori information on the endogenous buffers, pumps, or leaks present in the experimental system. The underlying concept is that the spatiotemporal series of the Ca²⁺ concentration inherently carries information of how the various processes at work affect its evolution, an

idea that is drawn from the theory of time-series analysis (Packard et al., 1980; Mindlin et al., 1990, 1998; Gouesbet, 1992). In this article we present a detailed description of the algorithm, and verify its accuracy by testing it with both numerically generated images and experimental confocal fluorescence images of Ca^{2+} flux through single voltage-gated channels expressed in *Xenopus* oocytes.

METHODS

The algorithm: basic assumptions

Fluorescence images provide information on the distribution of Ca^{2+}-bound dye, $[CaB]$. Given that we are interested in images obtained in oocytes, we assume that the dye only reacts with Ca^{2+} according to the kinetic scheme

$$Ca^{2+} + B \underset{k_{off}}{\overset{k_{on}}{\rightleftharpoons}} CaB, \quad (1)$$
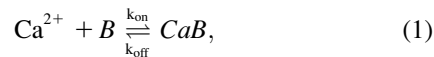
where k_{on} and k_{off} are the kinetic rate constants from which the dissociation constant, $K_d \equiv k_{off}/k_{on}$, is obtained. We assume that the dye, B, is initially distributed uniformly in space, that there are no dye sources or sinks during the time course of the experiment, and that its diffusion coefficient is not changed when Ca^{2+} binds to it. Then, the total dye concentration, $[B]_T = [B] + [CaB]$, remains equal to its uniform (known) initial value at any given time and spatial point. Thus, the evolution of $[CaB]$ is given by

$$\frac{\partial [CaB]}{\partial t} = -R + D_B \nabla^2 [CaB], \quad (2)$$

where D_B is the dye diffusion coefficient and R is the reaction term,

$$R = -k_{on}[Ca^{2+}]([B]_T - [CaB]) + k_{off}[CaB]. \quad (3)$$

We can compute the time and spatial derivatives of $[CaB]$ from the experimental records. In this section we will assume that they can be computed with perfect accuracy and discuss their errors later. Now, line-scan images only contain data along one spatial dimension, x. We then assume that the release of Ca^{2+} has spherical symmetry (this is satisfied, in particular, if the release occurs over a very small region that can be treated as a point), and that there is nothing else around that can break this symmetry. With these assumptions, the solution always has spherical symmetry (i.e., it only depends on time and the distance, r, from the site of release). If the line-scan goes through the center of the release region, we can compute $\nabla^2[CaB]$ using only the information along the direction, x. We analyze later what happens when the line-scan does not go exactly through the center of the release site. Calculating $\nabla^2[CaB]$ and $\partial[CaB]/\partial t$ we can obtain from Eq. 2 the value of R at every spatial point and time. Using Eq. 3, we can then obtain a spatiotemporal series of the variable of interest, $[Ca^{2+}]$. Up to this point, our method is similar to previous ones (Blatter et al., 1997). It is also similar to the method proposed recently in Soeller and Cannell (2002), although it differs in the fact that here we assume that the dye only binds to Ca^{2+}.

Upon its release Ca^{2+} diffuses, reacts with buffers, and is recaptured by different pumps. Of all these processes, we want to single out three—two for which we know some details, the reaction with the dye and diffusion; and the other that we want to compute, the Ca^{2+} source, Q_{Ca}. In this way we write the evolution equation for Ca^{2+} as

$$\frac{\partial [Ca^{2+}]}{\partial t} = R + D_{Ca} \nabla^2 [Ca^{2+}] + M + Q_{Ca}, \quad (4)$$

where D_{Ca} is the free diffusion coefficient of Ca^{2+} ($\sim 220 \ \mu m^2/s$, Allbritton et al., 1992) and the term M represents the sum of all the processes whose details are poorly known in each experiment, which usually depend on the peculiarities of the cell that is being observed. If we had a complete model of

the intracellular Ca^{2+} dynamics, then we would be able to write an expression for M, which would depend on other variables, such as the concentrations of the endogenous Ca^{2+} buffers and of the pumps (this is what is done in Blatter et al., 1997; Rios and Brum, 2002; Rios et al., 1999; Soeller and Cannell, 2002). Therefore, Eq. 4 would have to be solved coupled to evolution equations for these other variables (or, equivalently, as done in Blatter et al., 1997; Rios and Brum, 2002; Rios et al., 1999; Soeller and Cannell, 2002, once $[Ca^{2+}]$ is known as a function of space and time, the evolution equations for these other variables could be integrated, provided that we knew all the kinetic parameters and initial concentrations that, together with $[Ca^{2+}]$, determine their evolution). Unfortunately, when the information about the buffers, pumps, or leaks in the experimental condition is insufficient, it is not possible to write an accurate expression for M without introducing ad hoc assumptions. Even when this can be done, the model validation itself can be a difficult (if not impossible) task and usually, the model lacks universality.

As shown in Appendix 1, all the dependence of $M(r, t)$ on variables other than $[Ca^{2+}]$ can be recast in terms of the values of $[Ca^{2+}]$ at (r, t) and at other spatial points and previous times, (r', t'). Due to the dissipative and diffusive nature of the processes involved in M, the dependence with $[Ca^{2+}](r', t')$ becomes weaker as (r', t') gets further away from (r, t). Performing a series expansion around (r, t), we can rewrite M in terms of $[Ca^{2+}](r, t)$ and space and time derivatives of $[Ca^{2+}]$ of relatively low order. The distinguishing feature of our method is the assumption that M can be approximated by this type of ansatz and that its functional dependence can readily be determined from the data. Namely, we assume that M can be written as

$$M = g \frac{\partial [Ca^{2+}]}{\partial t} + f \nabla^2 [Ca^{2+}] + h |\nabla [Ca^{2+}]|^2 + k, \quad (5)$$

where g, f, h, and k are unknown functions of the free Ca^{2+} concentration, $[Ca^{2+}]$, to be determined by the algorithm. We see from Eq. 5 that there is no term of the form $\mathbf{v} \cdot \nabla[Ca^{2+}]$ (a term proportional to a first derivative with respect to the spatial coordinates). This is so because there is no privileged direction in the problem due to the assumption of the spherical symmetry. Thus, we have gone to second order in space, keeping those terms that respect the spherical symmetry.

Even if we insert Eq. 5 in Eq. 4, Eq. 4 still has the unknown that we want to determine: the Ca^{2+} source, Q_{Ca}. The fact that Ca^{2+} release is localized in space and time implies that Q_{Ca} vanishes away from the source and everywhere in space when Ca^{2+} release ceases. Thus, there are points of the experimental record where $Q_{Ca} = 0$ and M is then the only unknown term of Eq. 4. Using the ansatz (Eq. 5), we can obtain numerical approximations to the unknown functions g, f, h, and k from the points of the record where $Q_{Ca} = 0$. Once we have these functions, we then know M as a function of $[Ca^{2+}]$ and its derivatives. Therefore, the only unknown of Eq. 4 is now Q_{ca}. So, computing the various space and time derivatives that are needed at the points where $Q_{Ca} \neq 0$, we can obtain Q_{ca} from Eq. 4 simply by doing $Q_{Ca} = -R - D_{Ca} \nabla^2 [Ca^{2+}] - M + \partial[Ca^{2+}]/\partial t$. Implicit in this method is the assumption that the way in which the other processes affect the spatiotemporal behavior of $[Ca^{2+}]$ can be written uniformly throughout the cytosol as a function of $[Ca^{2+}]$ and its derivatives. This is equivalent to say that the distribution of pumps and the total buffer concentrations are uniform in the cytosol. These assumptions are always present in the backward methods used to obtain the Ca^{2+} current from fluorescent images.

The algorithm: numerical implementation

We now describe the algorithm we have developed following the ideas outlined in the previous section. It has six main steps. Fig. 1 shows an overview of the procedure. The images of Fig. 1 correspond to numerically generated experiments obtained by simulating Eqs. 15–17 with a source of the form (Eq. 19), with $R_f = 0.15 \ \mu m$, $t_s = 3$ ms, and $t_d = 10$ ms. The experiment on the top has $I = 0.1$ pA and the one on the bottom $I = 0.3$ pA.
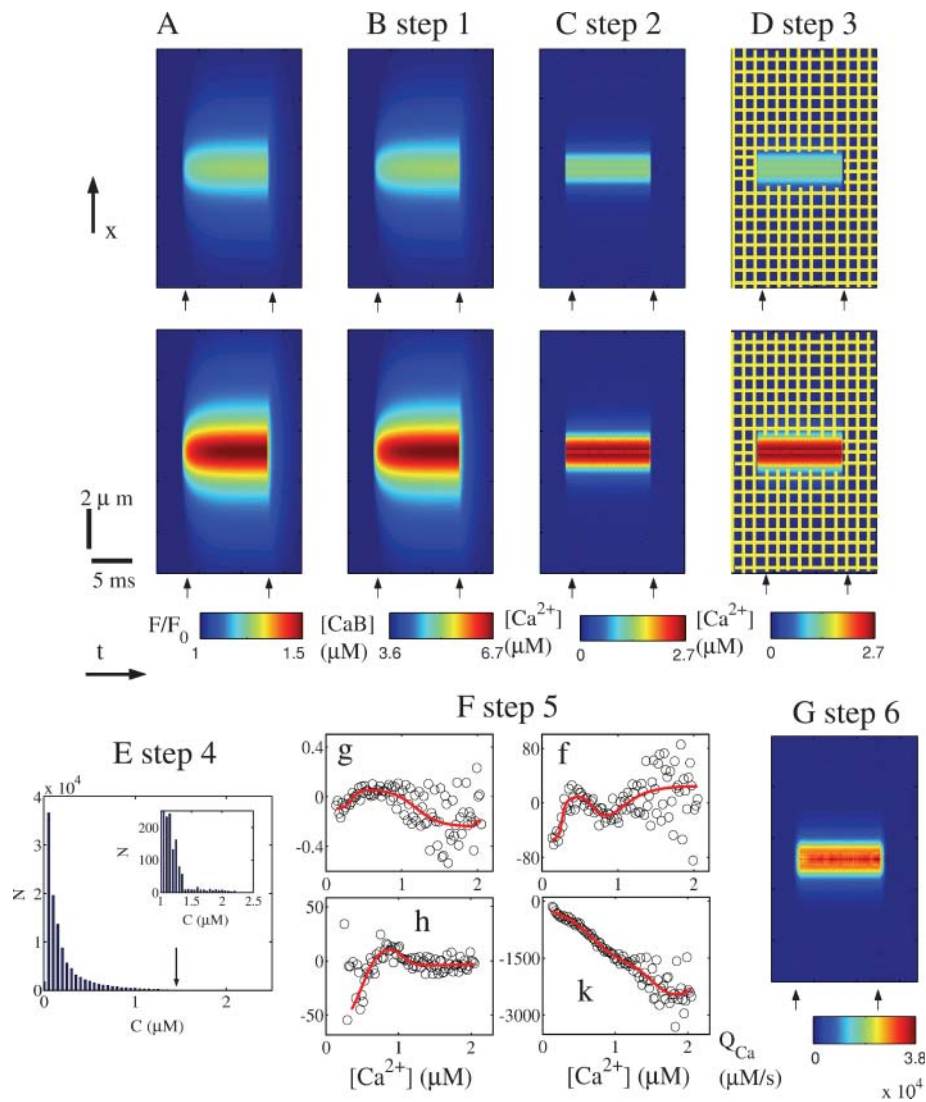
FIGURE 1 Outline of the main steps involved in the flux reconstruction algorithm. (*A*) Space-time plot of the fluorescence distribution of the two (numerically generated) experiments with which we are going to work. Both experiments are needed for the application of the algorithm but the calcium release flux will only be determined for the one on the top. (*B*) [*CaB*] is shown on the same space-time plot as in *A*. [*CaB*] is obtained from the fluorescence data using Eq. 6. (*C*) [Ca^{2+}] is shown on the space-time plot of *A*. [Ca^{2+}] is obtained from [*CaB*] using Eq. 8. (*D*) Same figure as in *C* but with a grid superimposed onto the regions where we assume that $Q_{Ca} = 0$. For illustration purposes, the grid that is drawn is much more sparse than the one that we actually use for our calculations (which would be undistinguishable on the scale of the figure). We compute *M* at each point in the gridded regions using Eq. 9. (*E*) In Step 4, the values of [Ca^{2+}] are binned according to Eq. 10 (in the example we use $N = 50$). We show in the figure the number of data points, (r_i, t_i), in the gridded regions of *D* as a function of C_i. At least four data points are necessary for each C_i to apply the method. (*F*) The functions *g* (dimensionless), *f* (in units of $\mu m^2/s$), *h* (in units of $\mu m^2/(\mu M/s)$), and *k* (in units of $\mu M/s$), as a function of [Ca^{2+}], obtained by interpolating the solution of the overdetermined system of the expressions in Eq. 11. Circles correspond to the solutions that minimize the merit function (Eq. 35) at each binned [Ca^{2+}] value (see Appendix 2). The smooth curves correspond to fits to the circles using fifth-degree polynomials. Knowing the smooth functions, we have an expression for *M* as a function of [Ca^{2+}] and its derivatives via Eq. 5, for all the values of [Ca^{2+}] that the experiment on the top of *A* attains. Inserting this expression in Eq. 4, we obtain the source distribution, Q_{Ca}, in space and time for this experiment as shown in *G*.

Step 1: obtaining [CaB] from fluorescence data

We assume that there is a linear relation between the fluorescence, *F*, and [*CaB*] of the form

$$[CaB](x_j, t_k) = [B]_T \frac{\dfrac{F(x_j, t_k)}{F_{min}} - 1}{\dfrac{F_{max}}{F_{min}} - 1}, \quad (6)$$

with $F(x_j, t_k)$ the fluorescence at pixel (j, k), of coordinates $x_j = j\Delta x$ and $t_k = k\Delta t$, where Δx and Δt are the spatial and temporal resolutions of the experiment, respectively, and the spatial coordinate *x* is the distance along the line-scan. F_{min} and F_{max} are the minimum and maximum values of the fluorescence corresponding to Ca^{2+}-free and Ca^{2+}-saturated dye. The ratio F_{max}/F_{min} can be determined, a priori, for each experimental condition. The meaningful information is contained in all the data points with either $x > 0$ or $x < 0$, given that the point $x = 0$ coincides with the center of the source. Thus, there is redundant information if the spherical symmetry assumption is

correct. We then average the information at each point $x > 0$ with the information from the corresponding negative value ($x < 0$) and work with a half-signal image.

Fig. 1 *A* shows the spatiotemporal evolution of the fluorescence, as typically obtained in line-scan images, for the two numerical experiments. Fig.1 *B* displays the distribution, [*CaB*], computed from Eq. 6 using the fluorescent distribution of Fig. 1 *A* after taking the average of *F* at plus and minus *x*, for each *x*. We use a pseudo-color scale to quantify concentration values: red corresponds to the highest concentration whereas blue corresponds to the basal one.

Step 2: obtaining the free calcium concentration

Once having [*CaB*], we obtain the reaction term *R* from Eq. 2,

$$R = D_B \nabla^2 [CaB] - \frac{\partial [CaB]}{\partial t}. \quad (7)$$

[Ca^{2+}](r, t) is computed using Eqs. 3 and 7,

$$[\text{Ca}^{2+}] = \frac{k_{\text{off}}[CaB] - R}{k_{\text{on}}([B]_{\text{T}} - [CaB])}. \qquad (8)$$

Notice that Eq. 8 contains a term of the form $[B]_{\text{T}} - [CaB]$ in the denominator. Therefore, the method will work provided that this term is away from zero, a condition that is met when the dye is not saturated. That is exactly the condition under which imaging experiments are done: dye saturation is avoided to follow $[\text{Ca}^{2+}]$ changes as closely as possible (e.g., compare the maximum value of $[CaB]$ in Figs. 1 and 7 with the total dye concentration, $[B]_{\text{T}} = 40 \ \mu\text{M}$). Also notice that obtaining R and $[\text{Ca}^{2+}]$ involves taking numerical derivatives with respect to time and space. As numerical differentiation is very sensitive to noise in the input data, filters might be used to minimize noise amplification. As explained before, for the calculation of the Laplacian we assume spherical symmetry around the center of the source.

Step 3: obtaining M away from the source

Using Eq. 4, $M(r, t)$ is determined locally in regions away from the Ca^{2+} source, i.e., where $Q_{\text{Ca}} = 0$. The gridded region shown in Fig. 1 D represents the region where we assume that no source is present. Thus, for the data points within this zone we have

$$M = \frac{\partial[\text{Ca}^{2+}]}{\partial t} - R - D_{\text{Ca}}\nabla^2[\text{Ca}^{2+}]. \qquad (9)$$

In the case of Fig. 1 we know that the Ca^{2+} source spreads over a region of radius 0.15 μm; it turns on at $t = 3$ ms and lasts for 10 ms. However, for experimental data, mild a priori assumptions about the spatiotemporal distribution of the release source must be made at this point, since the precise morphology of the source is not generally known. In these cases, we discard a region of the spatiotemporal record that overestimates the typical source size and duration, trying to keep enough data points in the gridded regions with concentrations different from basal. If there are N_{tot} data points within the gridded regions, we have N_{tot} equalities of the form (Eq. 9) from which we can obtain M as a function of (r, t) for values of r and t such that $Q_{\text{Ca}}(r, t) = 0$. As explained in the next step, N_{tot} needs to be relatively large for the algorithm to work.

Step 4: binning the values of $[Ca^{2+}]$ attained during a series of experiments

The previous step provides M as a function of (r, t) for values of r and t such that $Q_{\text{Ca}}(r, t) = 0$. However, we want M as a function of $[\text{Ca}^{2+}]$ and its derivatives so that we can use Eq. 5, the ansatz, to determine the four unknown functions of $[\text{Ca}^{2+}]$, f, g, h, and k. To this end, we compute the minimum, $[\text{Ca}^{2+}]_{\text{min}}$, and maximum, $[\text{Ca}^{2+}]_{\text{max}}$, values of $[\text{Ca}^{2+}]$, attained in regions with $Q_{\text{Ca}} = 0$ by the whole set of experiments that we are going to use (all data points in the gridded regions of Fig. 1 D). Then, we bin the interval $[[\text{Ca}^{2+}]_{\text{min}}, [\text{Ca}^{2+}]_{\text{max}}]$ in a finite set of values. Thus, we define a vector of free Ca^{2+} concentration values as

$$C_i = [\text{Ca}^{2+}]_{\text{min}} + \Delta C, \quad 1 \leq i \leq n, \qquad (10)$$

where $\Delta C \equiv ([\text{Ca}^{2+}]_{\text{max}} - [\text{Ca}^{2+}]_{\text{min}})/n$ and n is the number of bins of $[\text{Ca}^{2+}]$ values that we will consider. We then determine all the points, $\zeta_{\text{j,k}}(C_i) \equiv (r_{\text{j}}, t_{\text{k}})(C_i)$, in the gridded regions of the images such that $C_i \leq [\text{Ca}^{2+}](r_{\text{j}}, t_{\text{k}})(C_i) < C_{i+1}$. Clearly, there is more than one data point, $\zeta_{\text{j, k}}(C_i)$, for each value of C_i. This is illustrated in Fig. 1 E where we plot the total number of grid points, N (coming from all the experiments that are being used), whose $[\text{Ca}^{2+}]$ value is contained in the bin of concentration, C. As C increases, N decreases significantly. In particular, $N(C) \geq 4$, to be able to apply the algorithm. Therefore, all values of C such that $N(C) < 4$ are

discarded. The arrow in Fig. 1 E indicates this cutoff and the inset shows a zoom of the figure around the cutoff value in this example. As described later in further detail, the value of ΔC must be chosen so as to guarantee the applicability of the algorithm for a sensible range of $[\text{Ca}^{2+}]$ values.

Step 5: obtaining the functions g, f, h, and k

The binning of $[\text{Ca}^{2+}]$ reduces the functions f, g, h, and k to vectors defined as $f_i = f(C_i)$, $g_i = g(C_i)$, $h_i = h(C_i)$, and $k_i = k(C_i)$, $1 \leq i \leq n$. Therefore, we now seek approximations to these vectors. For each value of C_i, we have as many binned versions of Eq. 5 of the form

$$M(\zeta_{\text{j,k}}(C_i)) = g_i \frac{\partial[\text{Ca}^{2+}]}{\partial t}\Big|_{\zeta_{\text{j,k}}(C_i)} + f_i\nabla^2[\text{Ca}^{2+}]\Big|_{\zeta_{\text{j,k}}(C_i)}$$
$$+ h_i|\nabla[\text{Ca}^{2+}]|^2_{\zeta_{\text{j,k}}(C_i)} + k_i, \qquad (11)$$

as data points $\zeta_{\text{j, k}}(C_i)$. The only unknowns in Eq. 11 are f_i, g_i, h_i, and k_i, $1 \leq i \leq n$. Thus, to determine their values, we need at least four data points, $\zeta_{\text{j, k}}(C_i)$ for each i, $1 \leq i \leq n$. This imposes some constraints on the allowed values of ΔC. We choose ΔC so that the system (Eq. 11) is overdetermined (the number of data points, $\zeta_{\text{j, k}}(C_i) \geq 4$, for every i). In this way, f_i, g_i, h_i, and k_i may be found using standard minimization or singular value decomposition techniques (see Appendix 2). Once g_i, f_i, h_i, and k_i are found, a global fitting of each function dependence on $[\text{Ca}^{2+}]$ is performed (Fig. 1 F). To this end, we use a feedforward neural network which provides a nonlinear curve fitting in terms of hyperbolic tangents. This allows us to interpolate the value of M at any Ca^{2+} concentration within the range $[C_{\text{min}}, C_{\text{max}}]$. As explained in Results, below, when working with real experimental records, only a small proportion of the records has $[\text{Ca}^{2+}]$ values that lie beyond C_{max} and are used only for the estimation of the functions f, g, h, and k.

Step 6: calcium release reconstruction

Finally, once the functions g, f, h, and k are known, M can be computed at any spatial point and time using Eq. 5, even where and while there is release, since both $[\text{Ca}^{2+}]$ and its space and time derivatives are known at every data point, (r, t). Now, in a given experiment, $[\text{Ca}^{2+}]$ will be larger in the region with $Q_{\text{Ca}} \neq 0$ than in the region where there is no source. However, the collection of M values as a function of $[\text{Ca}^{2+}]$ and its derivatives is obtained in the region with $Q_{\text{Ca}} = 0$. If we use the data from one experiment with only one release event, we will not have direct information on the values of M for the larger $[\text{Ca}^{2+}]$ values that occur in the region with $Q_{\text{Ca}} \neq 0$. One possibility to overcome this difficulty is to extrapolate the functions, f, g, h, and k, to obtain estimates of their values for these larger $[\text{Ca}^{2+}]$, using the expressions obtained for the lower concentrations. The other possibility is to determine these functions using various spatiotemporal regions, coming either from around different release sites or from different experiments done on the same cell (as illustrated in Fig. 1 A, where the *upper image* corresponds to a low influx Ca^{2+} current and the *bottom image* to a higher current one). In this way, the information that comes from the region around the site with the largest release will be used only to determine g, f, h, and k. The algorithm will then be applied to obtain the release flux from the regions with smaller release. We mainly follow this last approach. In this way, we cannot obtain an estimate of what the underlying Ca^{2+} current is at the site of largest release. As discussed in Appendix 2, we obtained better current estimates setting $f = g = h = 0$ from the beginning and using only $k \neq 0$. All figures shown in the article, with the exception of Fig. 1, were done in this way.

Once we have M at every (r, t) for a particular experiment we can go back to Eq. 4 and solve for Q_{Ca},

$$Q_{\text{Ca}} = \frac{\partial[\text{Ca}^{2+}]}{\partial t} - R - D_{\text{Ca}}\nabla^2[\text{Ca}^{2+}] - M. \qquad (12)$$

Eq. 12 gives the source distribution in space and time in units of concentration per unit time, e.g., μM/s (Fig. 1 G). Integrating Q_{Ca} over the volume where it is non-negligible we can also obtain the number of Ca^{2+} ions that enter the region per unit time which, in turn, can be expressed as an electrical current, I, using the known information on the ion's charge. If $Q_{Ca}(r, t)$ is in μM/s, then the current could be obtained, in pA, as

$$I(t) = \gamma \int_0^{r_{source}} Q_{Ca}(r, t) 4\pi r^2 dr, \qquad (13)$$

where $\gamma = 1.92 \times 10^{-4}$ pC/μm^3 and we choose $r_{source}(t)$ so that

$$\int_{r_{source}}^{(1+\zeta)r_{source}} Q_{Ca}(r, t) r^2 dr \leq \kappa \int_0^{r_{source}} Q_{Ca}(r, t) r^2 dr, \quad (14)$$

with $\zeta = 0.5$, and $\kappa = 0.3$.

Numerical simulations

Most of the numerical simulations that we use to test the accuracy of the reconstruction method correspond to a model with Ca^{2+}, dye, and one extra buffer. The dye, B, and the extra buffer, E, react with Ca^{2+} according to a kinetic scheme like the one in Eq. 27 with reaction rates of k_{on}^B, k_{off}^B and k_{on}^E, k_{off}^E, respectively. Assuming that both the dye and the buffer are initially uniformly distributed in space and that the Ca^{2+} bound and the free corresponding buffer diffuse at equal rates, then the evolution equations are

$$\frac{\partial[Ca^{2+}]}{\partial t} = -k_{on}^B[Ca^{2+}]([B]_T - [CaB]) + k_{off}^B[CaB]$$
$$- k_{on}^E[Ca^{2+}]([E]_T - [CaE]) + k_{off}^E[CaE]$$
$$+ D_{Ca}\nabla^2[Ca^{2+}] + Q_{Ca} + q_{uptake}, \qquad (15)$$

$$\frac{\partial[CaB]}{\partial t} = k_{on}^B[Ca^{2+}]([B]_T - [CaB]) - k_{off}^B[CaB]$$
$$+ D_{CaB}\nabla^2[CaB], \qquad (16)$$

$$\frac{\partial[CaE]}{\partial t} = k_{on}^E[Ca^{2+}]([E]_T - [CaE]) - k_{off}^E[CaE]$$
$$+ D_{CaE}\nabla^2[CaE], \qquad (17)$$

where $[B]_T$ and $[E]_T$ are the dye and buffer total concentrations, D_{Ca}, D_{CaB}, and D_{CaE} are the diffusion coefficients of free Ca^{2+}, dye, and extra buffer, respectively, and q_{uptake} represents the Ca^{2+} uptake, which is given by (Soeller and Cannell, 2002)

$$q_{uptake} = \frac{k_1[Ca^{2+}]^m}{k_2^m + [Ca^{2+}]^m}. \qquad (18)$$

All parameters of the model are listed in Table 1 (the parameters of the dye B correspond to those of fluo-4 dextran, and the buffer E to those of EGTA). For some numerical experiments we take $k_1 = 0$. The set of expressions in Eqs. 15–17 is not a realistic model of Ca^{2+} dynamics inside a cell, but is useful to test the performance of the algorithm. For the Ca^{2+} release term, Q_{Ca}, we assume that it is different from zero on a sphere of radius R_f (0.15 μm $\leq R_f \leq$ 1.0 μm). The Ca^{2+} release time course is either a square step

$$Q_{Ca} = \begin{cases} \alpha I, & \text{if } r < R_f \quad \text{and} \quad t_s < t < t_s + t_d, \\ 0 & \text{otherwise,} \end{cases} \qquad (19)$$

or a step with an exponential tail,

TABLE 1 Parameters used in the simulations with dye and one extra buffer

Biophysical parameters		Computational parameters	
D_{Ca}	220 μm^2/s	Δr	0.01 μm
D_{CaB}	50 μm^2/s	Δt	10^{-7} s
D_{CaE}	113 μm^2/s	R_f	0.15–1.0 μm
$[Ca^{2+}]_{rest}$	0.05 μM	t_d	1–15 100^{-3} s
$[B]_T$	40 μM		
$[E]_T$	1000 μM		
k_{on}^B	100.0 μM^{-1} s^{-1}		
k_{off}^B	400.0 s^{-1}		
k_{on}^E	1.5 μM^{-1} s^{-1}		
k_{off}^E	0.3 s^{-1}		
k_1	200 μMs^{-1}		
k_2	0.184 μM		
m	3.9		

$$Q_{Ca} = \begin{cases} \alpha I, & \text{if } r < R_f \text{ and } t_s < t < t_s + t_d, \\ \alpha I \exp\left(-\frac{t - (t_s + t_d)}{\tau}\right) & \text{if } r < R_f \text{ and } t > t_s + t_d, \\ 0 & \text{otherwise,} \end{cases}$$
$$(20)$$

where $\alpha = 5.2 \times 10^3 \mu$M μm$^3/(4/3\pi R_f^3 pC)$, so that Q_{Ca} is in μM/s and I in pA. All these simulations were started from a uniform equilibrium distribution of all species at a resting Ca^{2+} concentration of 50 nM. The model equations were solved numerically using a finite difference scheme on a spherically symmetric grid, with spatial and temporal steps of 0.01 μm and 10^{-7} s, respectively.

For ideal conditions, the (numerically generated) fluorescence records were not blurred and represented an in-focus recording through the center of the release site. In a real experiment, each point of an image contains light coming from a region whose typical lengths, measured as full width at half-maximum, are $\Delta_{xy} \sim 300$ nm along the focal plane and $\Delta_z \sim 500$–700 nm in the direction perpendicular to the focal plane, z. On the other hand, the data acquisition system imposes limits on how often the data can be recorded: the spatial separation between two successive experimental points is ~ 150 nm. To study the influence of the microscope finite resolution and of the data collecting process, a coarse-graining procedure was applied to the numerically simulated signals. Namely, we computed a coarse-grained fluorescence, F, from the well-resolved numerically computed one, $\mathcal{F}$, at spatial points separated by $d = 150$ nm along the scanning line, ($x_k = k d, y = 0$, $z = 0$), by convoluting $\mathcal{F}$ with a Gaussian,

$$F(x_k, 0, 0, t) = \frac{1}{(2\pi)^{3/2}\sigma_{xy}^2\sigma_x} \int dx \, dy \, dz \, \mathcal{F}(x, y, z, t)$$
$$\times \exp\left[-\left(\frac{(x - x_k)^2 + y^2}{2\sigma_{xy}^2} + \frac{z^2}{2\sigma_z^2}\right)\right], \qquad (21)$$

where $\sigma_w = \Delta_w/\sqrt{(8\ln(2))}$ ($w = xy, z$). In some cases, to analyze the effects of the blurring process by itself, we applied Eq. 21 to each data point of the simulation (i.e., using d equal to the spatial resolution of the simulation instead of 150 nm). In certain cases, we also applied a deblurring procedure to the blurred data using the inverse of Eq. 21. We also analyzed the effect of noise of realistic amplitude on the application of the algorithm to numerical simulations. Namely, numerical simulations were performed as described before. The resulting data were subsequently blurred according to Eq. 21, keeping points with the space ($d = 0.15 \mu$m) and time ($\Delta t = 8$ ms) resolutions of the experiments. Noise with normal distribution of standard deviation 0.12 in units of the rescaled fluorescence (see Eq. 25) was then added to the blurred data. This amount of noise is similar to the one observed in the experimental records that we analyze in this article.

The assumption that the signal has spherical symmetry and that the scanning line, x, corresponds to a radial direction, holds only if the scanning line goes through the center of the release site. Although experimentally the focal plane is adjusted so that the release site belongs to it, there are always small errors and a certain offset, d_o, can be expected. To study how the algorithm performs if the scanning line does not go through the center of the release site, we took the results of the (spherically symmetric) simulations at a chosen distance or offset, d_o, from the center of the source to represent out-of-focus data. We then applied the algorithm to these out-of-focus numerically generated data.

Finally, we also performed some tests on a more realistic model of intracellular Ca^{2+} dynamics, more specifically, on a modified version of the model presented in Baylor et al. (2002) to describe Ca^{2+} sparks in frog skeletal muscle. The modifications we introduced are related to the way we deal with the dye and with the Ca^{2+} pump. First, we assume that the dye only binds Ca^{2+}. As it currently stands, our method cannot handle situations in which significant amounts of dye bind to proteins and fluoresce. Second, we use Eq. 18 for the Ca^{2+} uptake into internal stores (Soeller and Cannell, 2002). Other than that, we keep all the reactions considered in Baylor et al. (2002), as described in Table 2, and use a source of the form (Eq. 19) with $R_f = 0.15$ μm, $t_d = 10$ ms, and different values of I. The main goal of these simulations is to test the performance of the algorithm when several buffers of various kinetics are present and this modified model serves for this purpose.

Tests performed on the algorithm

In the cases of numerically simulated images the results of the algorithm can be readily compared with information that is available from the simulations. In particular, we compare the time course of the total current, $I(t)$, obtained from Eq. 13 and the time average of its magnitude,

$$\bar{I} \equiv \frac{1}{t_d} \int_{t_s}^{t_s + t_d} dt \, I(t), \qquad (22)$$

using the source predicted by the algorithm and the one used in the simulation. In the case of sources of the form (Eq. 19), we also compute the time average

$$\overline{Q_{ca}} \equiv \frac{1}{t_d} \int_{t_s}^{t_s + t_d} dt \, Q_{Ca}(r, t), \qquad (23)$$

using the source obtained with the algorithm and the one used in the simulation. This provides information on how well the algorithm determines the spatial spread of the source.

TABLE 2 Parameters and reactions of the model with various buffers

Constituent	Resting concentration	Diffusion constant
Free[Ca^{2+}]	0.05 μM	319 μm^2/s
Free[Mg^{2+}]	1000 μM	—
ATP	8000 μM	149 μm^2/s
Troponin	360 μM	0
Parvalbumin	1500 μM	15.9 μm^2/s
B	40–1000 μM	50 μm^2/s

Reaction	Forward rate	Reverse rate	K_D
$Ca^{2+} + ATP \rightleftharpoons CaATP$	15.6 μM^{-1} s^{-1}	34467 s^{-1}	2200 μM
$Ca^{2+} + B \rightleftharpoons CaB$	100 μM^{-1} s^{-1}	400 s^{-1}	4 μM
$Ca^{2+} + Parv \rightleftharpoons CaParv$	47.9 μM^{-1} s^{-1}	0.574 s^{-1}	0.012 μM
$Mg^{2+} + Parv \rightleftharpoons MgParv$	0.379 μM^{-1} s^{-1}	3.45 s^{-1}	91 μM
$Ca^{2+} + Trop \rightleftharpoons CaTrop$	101.7 μM^{-1} s^{-1}	132 s^{-1}	1.3 μM

Experiments

Experiments were performed on defolliculated *Xenopus laevis* oocytes expressing N-type voltage-activated Ca^{2+} channel from α_{1B-d} and β_3-subunits as previously described in Demuro and Parker (2003). Briefly, 2–4 days after mRNA injection, oocytes were injected with fluo-4 dextran (final intracellular concentration 40 μM) and 1 h later were placed in a chamber bathed in Ringer's solution including 6 mM calcium. Fluorescence signal was detected through a confocal pinhole providing lateral and axial resolutions of ~300 and 500 nm, respectively. Experiments were performed in line-scan mode (0.15 μm/pixel; 8 ms/line) and near-membrane images were constructed and analyzed using routines written in the IDL programming language. Membrane voltage was normally clamped at −60 mV using a conventional two-electrode voltage-clamp technique, and transient Ca^{2+} signals were evoked by stepping the oocyte membrane to more positive voltage than −25 mV. Strong polarization up to +30 mV evoked spatially homogeneous fluorescence signals that progressively become more localized and stepwise during weaker voltage steps approaching −25 mV. On the evidences presented in Demuro and Parker (2003) we consider these pulsatile signals to rise from Ca^{2+} influx through a single N-type Ca^{2+} channel and refer to them as *sparklets*.

All data presented here were obtained using fluo-4 dextran as the Ca^{2+} indicator. This low affinity dye showed a low fluorescence signal at basal cytosolic free [Ca^{2+}] and a large increase in fluorescence signal in the presence of high Ca^{2+} concentration, such that local fluorescence signals ($\Delta F/F$) of fivefold or greater could be produced. The parameters we considered for fluo-4 dextran (low affinity, $K_d \sim 4$ μM) are: $F_{max}/F_{min} \sim 20$ in the oocyte, $k_{on} = 100$ μM^{-1} s^{-1}, and $k_{off} = 400$ s^{-1}, whereas $D = 50$ μm^2 s^{-1}. Dye concentration in the oocyte was ~40 μM and resting Ca^{2+} concentration was considered to be [Ca^{2+}]$_{rest} \approx 50$ nM.

Processing of experimental signals

In the case of the experimental signals, the starting point (unless otherwise noted) is the smoothed-out fluorescent distribution that is obtained by averaging the raw one at each point of the space-time data file with its eight adjacent neighbors. We then compute the (theoretical) average basal fluorescence, F_b, inverting Eq. 6, using the basal concentration [CaB]$_b$ = [Ca^{2+}]$_b$[B_T]/(K_d+[Ca^{2+}]$_b$) that corresponds to [Ca^{2+}]$_b$ = 50 nM, K_d = 4 μM, and [B_T] = 40 μM. This gives

$$\frac{F_b}{F_{min}} = 1.23. \qquad (24)$$

We then compute the mean resting fluorescence at position x_j on the scan line, $\overline{F_{rest}}(x_j)$, as the time average of the fluorescence value at spatial point, x_j, before there is Ca^{2+} release. In the absence of inhomogeneities, and assuming that [Ca^{2+}]$_b$ = 50 nM before there is Ca^{2+} release, it should be $F_b = \overline{F_{rest}}(x_j)$ and this should be independent of (x_j); i.e., $\overline{F_{rest}}(x_j) = \langle \overline{F_{rest}} \rangle = F_b$. In any real experiment, this equality is only approximate. Thus, inserting $F_b/\overline{F_{rest}}(x_j) \approx 1$ in Eq. 24, we obtain

$$\frac{F(x_j, t_k)}{F_{min}} \approx \frac{F(x_j, t_k)}{\overline{F_{rest}}(x_j)} \frac{F_b}{F_{min}} = 1.23 \frac{F(x_j, t_k)}{\overline{F_{rest}}(x_j)}. \qquad (25)$$

We use this approximation to compute [CaB] from Eq. 6. The ratio $F(x_j, t_k)/\overline{F_{rest}}(x_j)$ in Eq. 25 is the rescaled fluorescence, F/F_0, which we display in the plots of the experimental signals.

To test to what extent the results of the algorithm are affected by the presence of noise, we smoothed out the experimental images even further using a nonlinear function fitting obtained with a feedforward neural network of the MATLAB Neural Network Toolbox (The MathWorks, Natick, MA). The parameters of the fitting, which can be written in terms of hyperbolic tangents, minimize the mean-square error between the smooth function and the data points. We compared the results obtained starting from these smoother images with those obtained starting from an image in which

only the eight-neighboring preprocessing had been done. We show that comparison in Results, below.

Error estimation

To estimate the error involved in Eq. 25, we compute the average resting fluorescence over all the pixels of the image, N_{pixels}, before Ca^{2+} release, $\langle F_{rest} \rangle \equiv \sum_j \sum_k (F(x_j, t_k)/N_{pixels})$, and its standard deviation, $\overline{\sigma_F} = (\sum_j \sum_k (F(x_j, t_k) - \langle F_{rest} \rangle)^2/N_{pixels})^{1/2}$. We assume that $\langle F_{rest} \rangle = F_b$. We then assume that the standard deviation of the basal fluorescence level, at any given point (before Ca^{2+} release), is given by $\sigma_F = \overline{\sigma_F}/\sqrt{N_{pixels}}$. Therefore, we assume that the error of approximating $F(x_j, t_k)/F_{min}$ by Eq. 25 is $F(x_j, t_k) /\overline{F_{rest}}(x_j)\sigma_F/F_{min}$. Furthermore, the measurement of the fluorescence itself always carries an error, ΔF. Taking these two sources of error into account and using Eqs. 24, 6, and $F_b = \langle F_{rest} \rangle$, these errors translate into an error in $[CaB]$ given by

$$\Delta[CaB] = \frac{1.23[B]_T}{\frac{F_{max}}{F_{min}} - 1}\left(\frac{F(x_j, t_k)}{\overline{F_{rest}}(x_j)}\frac{\sigma_F}{\langle F_{rest} \rangle} + \frac{\Delta F}{F_{rest}}\right). \quad (26)$$

For the experimental signals, we assume that the photon counting process is a Poisson process, so that the square of the standard deviation and the mean number of photons counted for an event of a given size are the same. Thus, we assume that $\Delta F/\sqrt{F} = \sigma_F/\sqrt{F_{rest}}$. Equation 26 with $\Delta F = \sigma_F\sqrt{F/F_{rest}}$ is the starting point for the error calculations in the case of the experimental signals. In the case of the noisy numerical simulations in which the normally distributed noise is added directly to the (blurred) $[CaB]$ distribution, we use Eq. 26 with $\Delta F/F_{rest} = 0.12$ and $\sigma_F = 0$. In the case of the noiseless numerical simulations we assume that $[CaB]$ has no errors.

Once $[CaB]$ is known, the next step of the algorithm requires the calculation of time and space derivatives. To calculate the first derivative of a function, Φ, at time t_i, we take a total of three data points, $\Phi(t_{i-1})$, $\Phi(t_i)$, and $\Phi(t_{i+1})$ and compute the slope of the straight line that gives the best fit to those three data points using least squares. In this way we also obtain an error associated to the derivative. Space and higher derivatives are computed similarly. These errors are then propagated so as to obtain the errors of all the quantities of interest. The fitting procedure in Step 5 of the algorithm introduces new errors. As explained in Appendix 2, this fitting is done by minimizing, for every binned Ca^{2+} concentration value, C_i—the sum of the square of the difference between the left- and right-hand sides of Eq. 11. As a result of this process, the errors in g_i, f_i, h_i, and k_i are determined in a standard way (see Appendix 2). These errors are then propagated so as to obtain an error in M which then propagates into an error for Q_{Ca} and, consequently, for the current that the algorithm gives.

Kinetic data obtained from the experimental records

The experimental records provide a visualization of Ca^{2+} release upon individual channel openings. Thus, given the time series of the reconstructed current, I, it is possible to obtain some kinetic information, such as the mean rising, open, and closing times of the channel. In this article we focus on the open time, t_o, which, for each event, we compute as $t_o = t_2 - t_1$ where $I(t_2) = I(t_1) = max\ I/2$, with $max\ I$ as the maximum value attained by the current during the event of interest. For comparison, we also compute it using the time series of the fluorescence averaged over a 0.45-μm region around the center of the release, as done in Demuro and Parker (2003).

RESULTS

Numerical tests of the reconstruction algorithm

We show here the results of applying the algorithm to numerically simulated images for which we know all the

details, so that we can compare the estimates that the algorithm gives with the actual values used in the simulations. In particular, we investigate how well the algorithm can determine the source size and geometry, the time course of Ca^{2+} release, and the total current. The numerical simulations were performed with the resolutions listed in Table 1. However, only points separated by 10^{-4} s in time were kept for the images and the reconstruction, unless otherwise noted.

Steplike single source

The first set of tests corresponds to simulations of Eqs. 15–17 with Ca^{2+} release of the form in Eq. 19. One such example is the one displayed in Fig. 1, for which $R_f = 0.15\ \mu$m, $t_s = 3$ ms, and $t_d = 10$ ms. We can observe in Fig. 1 G that the algorithm determines the spatial distribution of the Ca^{2+} source and its temporal time course quite well: the source fades away for radii greater than 0.15 μm and times larger than 13 ms. We can also observe that the fitted functions f, g, and h are relatively small for large enough $[Ca^{2+}]$, and that the individual values, f_i, h_i, and g_i, obtained for each binned $[Ca^{2+}]$ value are widely dispersed around the mean that the global fitting provides. For this reason, we tested the performance of the algorithm when we set f, g, and h exactly equal to zero obtaining current estimates that were 20% better (see Appendix 2). All the figures that we subsequently show in this article have been obtained in this way.

We show in Fig. 2 a plot of the magnitude of the reconstructed current obtained via Eqs. 13 and 22 as a function of the one used in the simulations, I, for simulations done with $R_f = 0.15\ \mu$m, $t_s = 3$ ms, and $t_d = 10$ ms. The slope of the linear fitting is 0.96 ± 0.04. This figure was done using simulations with I up to 3.9 pA.

We analyze now the algorithm's ability to distinguish between different source radii and step durations. To this end, we performed simulations with various source radii or
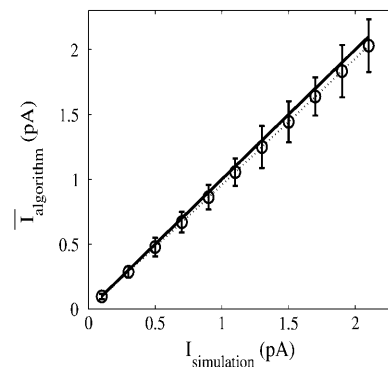

FIGURE 2 Application of the algorithm to data generated by numerical integration of Eqs. 15–17 with Eq. 19 as a source. The currents obtained with the algorithm are shown as a function of the ones used in the simulations. The best linear fit to these data of slope 0.96 ± 0.04 (*dotted line*) and the identity function are also plotted (*solid line*).

release duration and applied Step 6 to obtain Q_{Ca}, using the functions, g, f, h, and k obtained for similar simulations but with fixed $R_f = 0.15$ μm and $t_d = 10$ ms. We show in Fig. 3 A the current obtained with the algorithm and the one used in the simulations that were done with $I = 1$ pA, $R_f = 0.15$ μm, and three values of t_d. We observe that the algorithm captures very neatly the times at which the current is turned on (*upward arrow*) and off (*downward arrow*), providing a correct estimate of the release current. Similarly, we show in Fig. 3 B the ratio between the time average of the source obtained with the algorithm and the source amplitude used in the simulations that were done with $t_d = 10$ ms and three values of I and R_f keeping constant the magnitude of Q_{Ca}. We observe that the algorithm recognizes different source sizes and estimates their radii correctly. This test gives also a validation of our hypothesis that the functions g, f, h, and k do not depend on the source parameters, but only on the conditions of the environment surrounding the source.

Single source with exponential decay

The second set of tests corresponds to simulations of Eqs. 15–17 with Ca^{2+} release of the form in Eq. 20, $q_{uptake} = 0$, $R_f = 0.15$ μm, $t_d = 5$ ms, $I=1$ pA, and $\tau = 2$ ms. The aim here is to check how well the algorithm captures the temporal behavior of the source when it does not turn off abruptly. We show in Fig. 3 C the current used in the simulations (*solid line*) and the one obtained with the algorithm (*dotted line*). We observe that the algorithm does detect the exponential decay of the release estimating its time constant with $<1\%$ error, as shown in Fig. 3 D.

Steplike multi-opening source

We study now whether the algorithm can distinguish successive openings and closings of a single spherical source. Fig. 4 A shows the Ca^{2+} bound dye distribution from a simulation of Eqs. 15–17 with Ca^{2+} release of Eq. 19, with $R_f = 0.15$ μm, $I = 1$ pA but where the source opens and closes three times with pulse durations of 1, 2.5, and 1 ms, respectively. Between a closing and the successive opening no activity is present. In this case, only data points with $r > 0.15$ μm (at all times) were used to implement Steps 4 and 5 of the algorithm. Fig. 4 B shows the reconstructed source where it can be seen how well the algorithm distinguishes between active and inactive regions. The algorithm also recognizes the three successive openings as well as the pulse durations, as can be observed in Fig. 4 C, where the current obtained with the algorithm (*dotted line*) is compared with the one used in the simulation (*solid line*). As is apparent from the figure, the current magnitude is estimated with the same accuracy regardless of the duration of the release event.

Effects of defocusing and optical blurring

We show in Fig. 5 A the results obtained when we apply the algorithm to out-of-focus numerically generated data (data with an offset, d_o). The simulations are done with the same parameters as in Fig. 2. (*Circles* correspond to in-focus results, $d_o = 0$, slope $= 0.96 \pm 0.04$; *squares* to $d_o = 0.0707$ μm, slope $= 0.81 \pm 0.04$; *diamonds* to $d_o = 0.1118$ μm, slope $= 0.71 \pm 0.04$; and *asterisks* to $d_o = 0.1414$ μm, slope $= 0.50 \pm 0.03$. The *solid line* is the identity function, $I_{algorithm} = I_{simulation}$.) As expected, the reconstructed current becomes smaller as d_o increases. However, this trend is mitigated when a realistic blurring is added (using Eq. 21 with $\Delta_{xy} = 0.3$ μm, $\Delta_z = 0.7$ μm, and $d = 0.01$ μm). We show in Fig. 5 B a comparison of the curves we obtain with no defocusing or blurring (*circles*); with realistic blurring only (*squares*); with blurring and defocusing with $d_o = 0.1414$ μm (*triangles*); and with only defocusing with $d_o = 0.1414$ μm (*asterisks*). The slopes in this case are 0.96, 0.85, 0.71, and 0.50, respectively. When we work with real images that are generated by highly localized sources, we can address the problem of having some offset by preanalyzing the
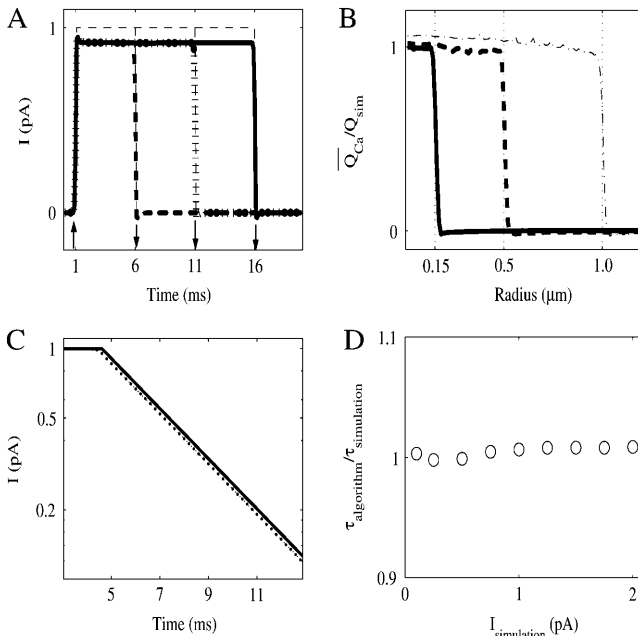

FIGURE 3 Algorithm's ability to distinguish different source parameters. The simulated data correspond to Eq. 19 (*A* and *B*), or to Eq. 20, with $R_f = 0.15$ μm, $t_d = 5$ ms, $\tau = 2$ ms, and $k_1 = 0$ (*C* and *D*). (*A*) Currents as a function of time, obtained with the algorithm (*thick dashed*, *dash-dotted*, and *solid lines*) and used in the simulations (*thin dashed lines*). Simulations done with $I = 1$ pA, $R_f = 0.15$ μm, and $t_s = 1$ ms (indicated by an *up-arrow*), and $t_d = 5$, 10, and 15 ms, respectively (indicated by *down-arrows*). (*B*) Ratio between the time average of the source obtained with the algorithm, $\overline{Q_{Ca}}$, and the source amplitude used in the simulation, as a function of space. Simulations done with $t_d = 10$ ms and $I = 0.1$ pA and $R_f = 0.15$ μm; $I = 3.7$ pA and $R_f = 0.5$ μm; and $I = 29.6$ pA and $R_f = 1$ μm, respectively (source radii indicated by *thin dotted lines*). (*C*) Current used in the simulation (*solid line*) and obtained with the algorithm (*dotted line*), as a function of time, for a case with exponential decay and $I = 1$ pA. (*D*) Ratio between the decay time constants obtained with the algorithm and those used in the simulations as a function of I.
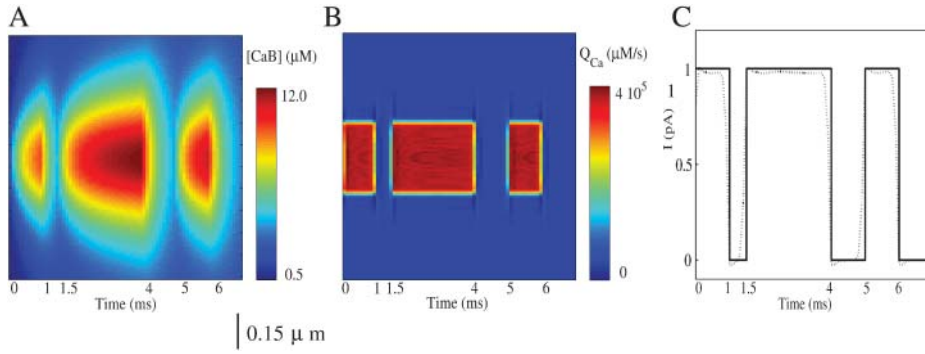
FIGURE 4 Algorithm's ability to recognize successive openings and closings of the source. The simulated data correspond to Eq. 19, with $R_f = 0.15$ μm, $I = 1$ pA, and $t_s = 0$, $t_d = 1$ ms; $t_s = 1.5$ ms, $t_d = 2.5$ ms; $t_s = 5$ ms; and $t_d = 1$ ms, respectively. (*A*) Distribution of calcium bound dye from the simulation. (*B*) Reconstructed source. (*C*) Currents used in the simulations (*solid line*) and reconstructed ones (*dotted line*), as a function of time.

distribution of $[Ca^{2+}]$. The stationary solution of the diffusion equation for $[Ca^{2+}]$ in the presence of a point source of current, I, located at the origin, is given by $[Ca^{2+}]_s = 414(I/D_{Ca}r)(\mu M\ \mu m^3/pC)$. If we take a line-scan of this solution along the x direction with no offset, then the distribution $[Ca^{2+}]_s(x)$ for $y = 0 = z$ is highly localized around $x = 0$. If we take the line-scan with an offset $d_o \equiv \sqrt{y^2 + z^2}$, the

half-width of $[Ca^{2+}]_s(x)$ is $\sqrt{3}d_o$. Thus, if we are trying to reconstruct sources that are contained within one pixel of the image, then whenever we obtain a distribution of $[Ca^{2+}]$ whose half-width is larger than two pixels, we can conclude that the offset is larger than the pixel size. Thus, we can use this preprocessing to either put some bounds on the offset or to discard certain images.
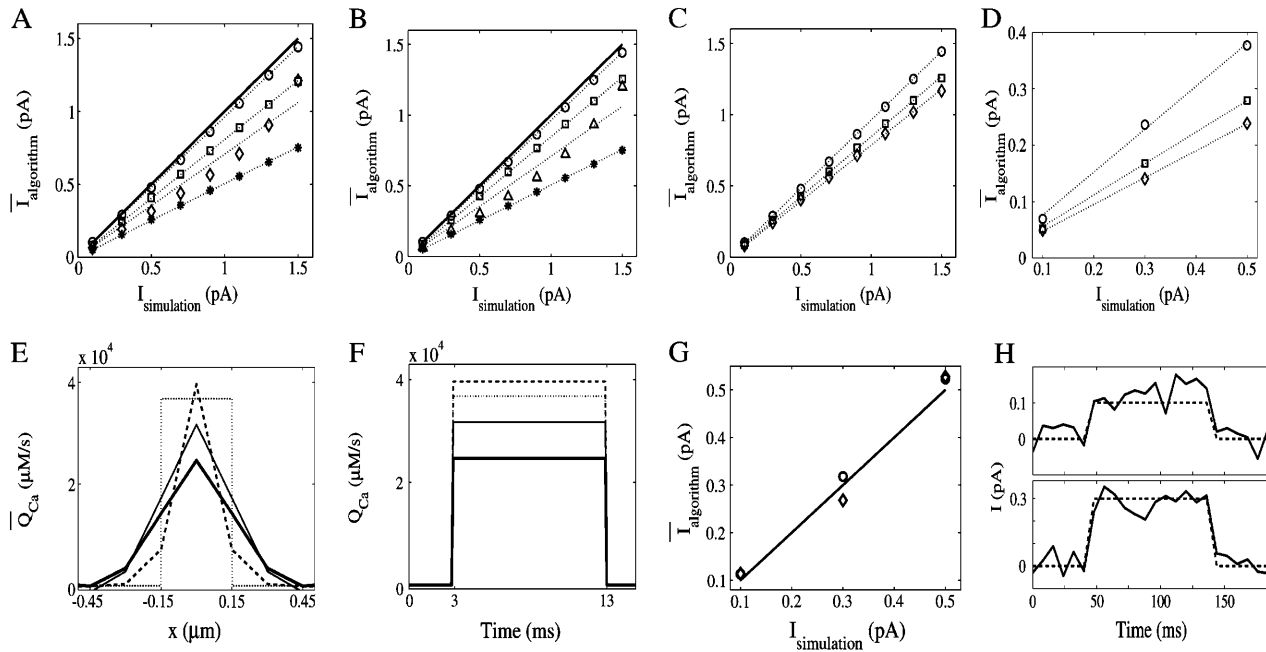

FIGURE 5 Effects of defocusing, blurring, finite space and time resolution, and noise on the reconstructed current. The simulations correspond to Eq. 19, with $R_f = 0.15$ μm, $t_d = 10$ ms (except for *G* and *H*, where $t_d = 100$ ms), and different values of I. The optical blurring was simulated using Eq. 21 with different values of Δ_{xy} and Δ_z. Only the simulations in *G* and *H* have added noise. (*A*) Effects of defocusing without blurring. The offsets are $d_o = 0$ (*circles*), $d_o = 0.0707$ μm (*squares*), $d_o = 0.1118$ μm (*diamonds*), and $d_o = 0.1414$ μm (*asterisks*). The solid line is the expected value for the current. (*B*) Effects of blurring and defocusing combined. Results with no defocusing or blurring (*circles*), with realistic blurring only (*squares*), with blurring and defocusing of $d_o = 0.1414$ μm (*triangles*), and with only defocusing of $d_o = 0.1414$ μm (*asterisks*). (*C* and *D*) Effects of blurring and spatial resolution without defocusing. Results with zero blurring (*circles*), with $\Delta_{xy} = 0.3$ μm, $\Delta_z = 0.7$ μm (*squares*), and with $\Delta_{xy} = 0.5$ μm, $\Delta_z = 0.9$ μm (*diamonds*). In *C* all the data points of the simulation were used, whereas only points separated by 0.15 μm were used in *D*. The slopes of the best linear fits are 0.96 (*circles*), 0.85 (*squares*), 0.78 (*diamonds*) in *C* and 0.76 (*circles*), 0.56 (*squares*), 0.48 (*diamonds*) in *D*. (*E*) Time-average of the source used in a simulation as a function of the line-scan coordinate (*thin solid line*), and corresponding ones obtained by applying the algorithm to the simulated data after it had been blurred using Eq. 21 with $d = 0.15$ μm (*thick solid line*), and after it had been subsequently deblurred by application of the inverse of Eq. 21 (*dashed line*). (*F*) Similar to *E*, but for $Q_{Ca}(x = 0)$ as a function of time. (*G*) Effects of noise and finite temporal resolution on the magnitude of the reconstructed current. Comparison of results with realistic blurring, finite space and time resolutions without noise (*circles*) and with noise (*diamonds*). The solid line is the expected value for the current. (*H*) Effects of noise and finite temporal resolution on the time course of the reconstructed current. Reconstructed currents (*solid lines*) and profiles used in the simulations (*dashed lines*) for an example with 0.1 pA (*upper panel*) and one with 0.3 pA (*lower panel*).

We show in Fig. 5, *C–F*, the effects of the optical blurring and of the finite space resolution when there is no offset. The simulations are done as before, but are subsequently blurred according to Eq. 21. In the applications of Fig. 5 *C* we keep all points of the simulation (x_k with $d = 0.01$ μm in Eq. 21), and in the rest, we keep points every 0.15 μm, to mimic the spatial resolution of the experimental acquisition system. Since fewer data points are available when $d = 0.15$ μm, only a subset of the currents reconstructed in *C* can be reconstructed in *D*. In Fig. 5, *C* and *D*, the reconstruction algorithm is applied directly to the blurred data with no previous deblurring. (*Circles* correspond to clean data; *squares* to $\Delta_{xy} = 0.3$ μm, $\Delta_z = 0.7$ μm, i.e., the expected blurring in the real experiments; and *diamonds* to $\Delta_{xy} = 0.5$ μm, $\Delta_z = 0.9$ μm.) In all cases the relationship between the reconstructed and the actual current is approximately linear with slopes of 0.96 and 0.76 (*circles*), 0.85 and 0.56 (*squares*), and 0.78 and 0.48 (*diamonds*), in *C* and *D*, respectively. In the case of the realistic blurring we also applied the algorithm after having applied a deblurring procedure obtaining a linear relationship of slope 0.99 for $d = 0.01$ μm and 0.73 for $d = 0.15$ μm (data not shown). Thus, the realistic blurring changes the slope only slightly (from 0.96 to 0.85) if the high resolution of the numerical simulation is kept. The slope changes by ~30% when only data with the expected resolution of a real experiment is kept ($d \sim 0.15$ μm) and the algorithm is applied directly to the blurred data. However, by a previous deblurring of the data, we obtain a slope that differs by only 4% from the one obtained using the high-resolution clean data. In the case of the experimental signals, we do not apply any deblurring procedure since that introduces too much noise and, as shown in Fig. 5 *B*, if there is an offset, working with the blurred image could give better estimates of the current.

We show in Fig. 5 *E* the time average of the source used in the simulation (*dotted line*), and the ones obtained by applying the algorithm to the simulated clean data with $d = 0.15$ μm (*thin solid line*), to the simulated data after it had been blurred using Eq. 21 with $d = 0.15$ μm (*thick solid line*), and to the same data but after it had been deblurred by application of the inverse of Eq. 21 (*dashed line*). We also applied the algorithm to previously deblurred data, keeping all the data points of the simulation, obtaining a source that is indistinguishable from the one obtained using clean data (data not shown). We then conclude that the difference between the source obtained from clean data (*thin solid line*) and the one obtained from blurred-deblurred data (*dashed line*) is a consequence of the 0.15 μm space resolution. Fig. 5 *F* is similar to *E*, except for Q_{Ca} being at the center of the release region ($x = 0$) as a function of time. The dotted line corresponds to the simulated source and the thin solid line to the one obtained by applying the algorithm to the clean simulated data. We observe in Fig. 5 *F* that the algorithm slightly overestimates the value of $Q_{Ca}(x = 0)$, but that this is compensated by an underestimation in other spatial points.

We can also observe that the spatial distribution of the source is the feature that differs the most between the reconstructed source and the one used in the simulation. The temporal profile, on the other hand, including both the times at which the source is turned on and off, are very well captured by the reconstruction algorithm in all cases.

Effects of noise and finite time resolution

Fig. 5, *G–H*, shows the effects of noise and finite time resolution when there is realistic blurring and no offset. The simulations are done as in Fig. 5, *C–F*, blurring the simulated data with $\Delta_{xy} = 0.3$ μm, $\Delta_z = 0.7$ μm, and keeping points every 0.15 μm in space and every 8 ms in time. The noisy data correspond to the addition of normally distributed noise to the blurred fluorescence, as explained in Methods, above. We show in Fig. 5 *G* the magnitude of the reconstructed currents as a function of the ones used in the simulations when the algorithm is applied to noiseless (*circles*) and to noisy (*diamonds*) data. The slopes are 1.05 ± 0.08 and 1.02 ± 0.18, respectively. The solid line is the identity function. As can be seen, there are no significant differences in the magnitude of the reconstructed currents for the noiseless and noisy cases. It must be noted that the current estimation is improved with respect to that of Fig. 5 *D* because the criterion given by Eq. 14 prescribes a larger value of $r_{source}(t)$ for the data with 8-ms time-resolution. Fig. 5 *H* shows two examples in which the magnitude and time course of the currents obtained with the algorithm when applied to the noisy data (*solid lines*) can be compared with the ones used in the simulations (*dashed lines*). The release events can be distinguished in both cases, although the uniform noise level that we have added, which is relatively large in the regions with low [Ca^{2+}], smears some of the release events in the case with 0.1 pA.

Effects of the presence of endogenous buffers with different kinetics

We study now the performance of the algorithm when applied to a model with several endogenous buffers of different kinetics. We use the model of Baylor et al. (2002) with the modifications described in Methods, above, and the parameters of Table 2, with [Ca^{2+}]$_{basal}$ = 0.05 μM always, regardless of the total amount of dye used. This is a model with very large amounts of ATP and Parvalbumin, which results in a fast capture of Ca^{2+}. In all cases, the algorithm is able to determine the duration and spatial spread of the source as accurately as in the cases illustrated in Fig. 3 (data not shown). However, due to the effective Ca^{2+} buffering by ATP and Parvalbumin, the Ca^{2+} current can be more or less underestimated, depending on the dye concentration. We show in Fig. 6 a plot of the currents that the algorithm gives as a function of the ones used in the simulations for different values of the total dye concentration. We observe that, for

a total dye concentration, $[B]_T = 40~\mu$M, the estimated current is 67% of the simulated one (*solid squares*) and for $[B]_T = 1$ mM (*asterisks*), the current is 74% of the simulated one. If $[B]_T$ is not large enough, the dye cannot compete with all the buffers and it is unable to sense the fast $[Ca^{2+}]$ changes that follow release. Since the algorithm relies on information that can be extracted from $[CaB]$, the released current is underestimated. However, if the $[Ca^{2+}]$ concentration dynamics can be described correctly by Eq. 4 with M given by the ansatz (Eq. 5), then the form of the functions f, g, h, and k should be independent of the properties of the dye (including its total concentration) and of the release, Q_{Ca}. However, when the dye cannot sense the fast variations of $[Ca^{2+}]$, the functions f, g, h, and k obtained from its corresponding $[CaB]$ are not determined correctly and do change with these properties. This results in a poorer determination of the $[Ca^{2+}]$ current, for which a correction factor could be estimated by analyzing the change of the functions f, g, h, and k with properties from which they should be independent. If the functions are correctly determined, we expect the algorithm to give a relatively good estimate of the $[Ca^{2+}]$ current. To check this, we used the functions obtained for $[B]_T = 1$ mM to analyze the simulations done with other values of $[B]_T$. Namely, we applied Steps 1–5 of the algorithm to the set of numerically simulated images generated with $[B]_T = 1$ mM and determined the function k (we set $f = g = h = 0$). We then used this function to approximate M (Eq. 5) and, using this expression for M, we applied Step 6 of the algorithm to the numerically simulated images generated with $[B]_T = 40$
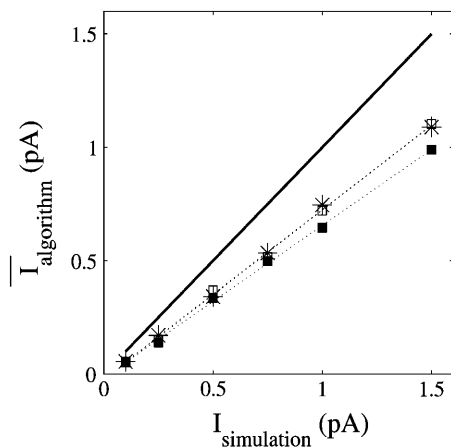
μM. We show in Fig. 6 the currents we obtain in this way as a function of the ones used in the ($[B]_T = 40~\mu$M) simulations (*open squares*), which can be fitted by a linear relation of slope 0.74. The improvement in the current value determination (from 67 to 74% of the actual one) means that the ansatz (Eq. 5) may capture the dynamics of the poorly known processes, even in the presence of various buffers of different kinetics, but that the functions that define it can only be determined with the necessary accuracy if the dye concentration is large enough to sense the fastest $[Ca^{2+}]$ changes.

Flux reconstruction of experimental calcium signals

We now describe the results of applying the algorithm to experimental Ca^{2+} signals (i.e., *sparklets*) obtained by averaging over eight neighbors of the spatiotemporal record, as described in Methods, above. Fig. 7 *A* illustrates sparklets arising autonomously at a localized site in response to a weak (–20 mV) depolarization that gives a low probability of channel opening (Demuro and Parker, 2003). The box indicates the region of the image whose analysis we describe in detail in the rest of the figure. We performed Steps 1–5 of the reconstruction algorithm on images containing 20 sparklets. We used the spatial (0.15 μm) and temporal (8 ms) resolution of the microscope and obtained Q_{Ca} (Step 6) for 17 of them. The maximum $[Ca^{2+}]$ of the three records for which Q_{Ca} could not be obtained were 7.01 μM, 10.79 μM, and 18.58 μM, whereas the maximum $[Ca^{2+}]$ value over the rest of the records was 5.25 μM and the functions f, g, h, and k could be determined up to $[Ca^{2+}] = 6.2~\mu$M. We could have determined the functions up to this $[Ca^{2+}]$ value even if we had not used the record that reached $[Ca^{2+}] = 18.58~\mu$M. This shows that the maximum $[Ca^{2+}]$ value of the records for which the current can be inferred are of the order of half the maximum value of those that are only used for the determination of the functions f, g, h, and k. This implies that this feature of the algorithm is not too restrictive, since larger fluctuations in peak fluorescence have been observed both in cardiac sparks (Izu et al., 2001) and in oocyte puffs (Sun et al., 1998). In our application, the number of records for which Q_{Ca} cannot be determined is a small proportion of the total number of records used. There are other limitations imposed by the experimental setup. The spatial extent of the source cannot be resolved since the pore size of an N-type Ca^{2+} channel is smaller than 1 nm (Hille, 2001) and the spatial resolution of the experiment is ∼150 nm. Regarding possible offsets, we preanalyzed the $[Ca^{2+}]$ distribution for the images and determined that in most of them the half-width of $[Ca^{2+}]$ was two pixels, with a few in which it was three. Taking into account that the optical blurring can enlarge the apparent source size by one pixel (given that the pixel size, ∼0.15 μm, is of the order of half the full-width of the blurring box, i.e., $\Delta_{xy} \sim 0.3~\mu$m) we think that, if there is

FIGURE 6   Application of the algorithm to numerical simulations of the model of Table 2, with Eq. 19 as its source, with $R_f = 0.15~\mu$m, $t_d = 10$ ms, and various values of I. The reconstructed currents are shown as a function of those used in the simulations for cases with $[B]_T = 40~\mu$M (*squares*) and $[B]_T = 1000~\mu$M (*asterisks*). Solid squares correspond to applying the algorithm using the function k determined from the simulations with $[B]_T = 40~\mu$M and open squares to using the function determined from the simulations with $[B]_T = 1$ mM. The best linear fits to these data of slopes 0.67 and 0.74 (*dotted lines*) and the identity function are also plotted (*solid line*). For clarity, the errors of the currents (∼15%) are not shown.
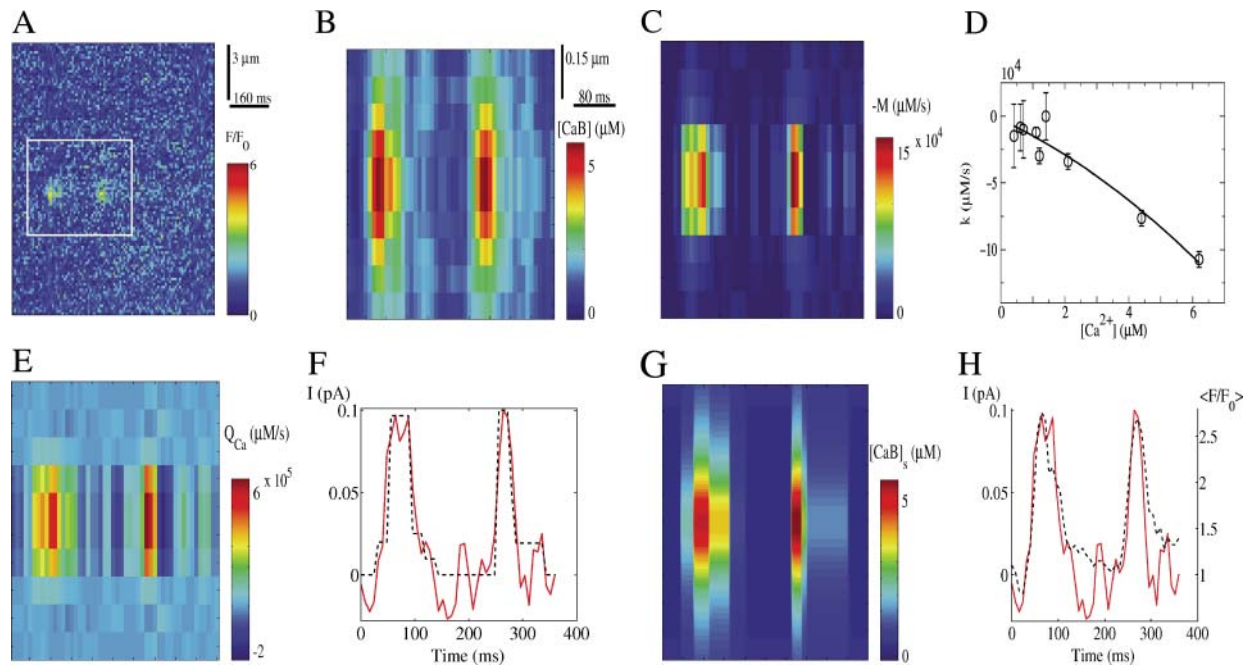
FIGURE 7 Experimental sparklets. (A) Line-scan image illustrating single channel events (sparklets) that arise in response to a 3-s-long depolarizing pulse. (B) Spatiotemporal spreading of the calcium-bound dye for the events in the box indicated in A. The scale bars in B are also valid for C, E, and G. (C) Spatiotemporal, M. (D) The curve $M = k([Ca^{2+}])$ and its smooth fitting. (E) Source obtained by the algorithm. (F) Temporal profiles of the reconstructed current that the algorithm predicts obtained by volume integration (Eq. 13) over a semispherical region of radius $r \sim 0.225$ μm (solid line) and of the one derived from the simplified, piecewise constant source, Q_{Ca}, used in the forward integration of the evolution equations (dashed line). (G) Spatiotemporal distribution of the Ca^{2+}-bound dye complex, $[CaB]_s$, obtained by numerical integration of Eq. 4 with $M(Ca^{2+})$ given by the smooth curve shown in D and the simplified source from which the dashed curve of F is obtained. (H) Temporal profile of the reconstructed current (solid line) and of the measured fluorescence averaged over a 0.45-μm region around the center of release (dashed line). For clarity, the error of the reconstructed current ($\sim$27%) is not shown.

any offset during the acquisition process, then it is not much larger than the pixel size. Fig. 7, B and C, display the spatiotemporal distribution of the Ca^{2+}-bound dye complex, $[CaB]$, and of the term $-M$, determined by the algorithm, respectively. Fig. 7 D contains the curve $M = k([Ca^{2+}])$ and its smooth fitting and Fig. 7 E shows the reconstructed source, Q_{Ca}. Comparing Fig. 7, C and E, we observe that $-M$ is $\sim$25% of the source term, Q_{Ca}, at least in the regions where Q_{Ca} is non-negligible. Using the smooth fitting shown in Fig. 7 D and a simplified, piecewise constant (in space and time), Q_{Ca}, chosen so as to give a similar mean current as the one given by the algorithm (see Fig. 7 F), we performed a forward integration of Eq. 4. The spatiotemporal distribution of the Ca^{2+}-bound dye complex, $[CaB]_s$, obtained in this way is shown in Fig. 7 G. Even though the forward integration does not have any added noise and the simplified version of the Ca^{2+} source is limited by the time and space resolution of the experimental record (see Fig. 7 F), the $[CaB]_s$ distribution compares reasonably well with the one obtained directly from the experimental record, $[CaB]$, both in magnitude and in time and space behavior. The full width at half-maximum of both distributions differ by $\sim$10 ms when looking at the time spread, and by $\sim$0.2 μm when looking at the spatial spread. Both differences are very close to the time (8 ms) and space (0.15 μm) resolutions

of the experimental records (and are <30% of the experimental full widths). The differences in the maximum values attained, on the other hand, are $\sim$14% and $\sim$6% for each of the release events depicted in Fig. 7.

Fig. 7 H displays the temporal profile of the fluorescence averaged over a 0.45-μm region (three pixels) centered around the point of release (dashed line) and of the reconstructed current, I, obtained from Q_{Ca} by volume integration (Eq. 13) over a semispherical region of radius $r \sim 0.225$ μm (solid line). For comparative purposes, the way the dashed curve is computed is similar to the way the data are processed in Demuro and Parker (2003)—i.e., as a plain average of the three points. The maximum current obtained with our algorithm along the time course of each event is within the values that are expected by extrapolation of the patch-clamp data obtained using Ba^{2+} instead of Ca^{2+} as the carrier (Demuro and Parker, 2003). In fact, by application of the algorithm to the 17 sparklets studied we obtain a mean current $I = (0.139 \pm 0.012)$ pA with a standard deviation of 0.040 pA. Given our previous results, this mean value could be a lower bound of the actual current, depending on the accuracy with which the functions f, g, h, and k can be determined. The effect of offset on this value should not be as acute as in Fig. 5, because the mean is an average over 17 events, most likely, with different offsets and, in several

cases, with an offset that is contained in the same pixel as the center of release. If we correct it by the factor we obtain in the case with blurring and an ~ 0.14-μm offset, this current estimate becomes 0.2 pA, of the order of the upper bound of previous estimations (Demuro and Parker, 2003). This, together with the results of the forward integration shown in Fig. 7 G, is an indication that, in this case, the ansatz (Eq. 5) is correctly determined from the data. To check this assertion, we also reanalyzed all the records using the function k determined by applying Steps 1–5 of the algorithm (setting $g = f = h = 0$) to two subsets of the experimental images, each one containing events of different duration. Neither the functions nor the estimated current changed significantly (we obtained $I = (0.130 \pm 0.012)$ pA and $I = (0.135 \pm 0.010)$ pA using each subset). Regarding the temporal profile of the current, although we do not obtain a perfectly square shape, we can observe in Fig. 7 H that the timescale of variation of the fluorescence when Ca^{2+} release starts or ends is (slightly) slower than that of Q_{Ca} or I. This sharper time-resolution of the reconstructed current also allows a better determination of the mean open time of the channel, which is closer to the value obtained from patch-clamp experiments. In particular, we show in Fig. 8 a plot of the open time, t_o, computed using the time course of the fluorescence averaged over three pixels ($t_o(F)$) as a function of the one computed using the reconstructed current ($t_o(I)$). We can roughly relate both times linearly with a slope 1.58 $\pm$ 0.55. As described in Demuro and Parker (2003), the events that can be observed with this optical technique are contained in the tail of the distribution of open times (i.e., very brief events are unobservable). By doing statistics over many events it is still possible to adjust the observations by an exponential distribution that gives information on the mean open time of the whole population of events (Demuro and Parker, 2003). We cannot perform such statistical

analysis directly on our data because we do not have a sufficient number of events. However, by using the linear relationship $t_o(F) \sim 1.58\ t_o(I)$, we can transform the mean open time, $t_o(F)$, obtained in Demuro and Parker (2003) into a mean open time for the current. We obtain $t_o(I) \approx (17.8 \pm 6.2)$ ms, which is closer to the one obtained with patch-clamp experiments, $t_o = 11.5$ ms (Demuro and Parker, 2003).

The results displayed in Figs. 7 and 8 were obtained starting from records in which the acquired data had been averaged over eight adjacent neighbors. This smoothing procedure is very mild and the image remains quite noisy. To put bounds to the errors that the noise introduces when the algorithm is applied to real experimental data, we have applied a second (stronger) smoothing procedure to the records before applying the algorithm, as explained in Methods, above. We show in Fig. 9 A the temporal profiles of the fluorescence for the noisy (*thin lines*) and the smooth (*thick lines*) records, and in Fig. 9 B those of the currents obtained by applying the algorithm to both types of records. We show in Fig. 9 C the maximum current obtained using the smooth records ($max(I_s)$) as a function of the maximum values obtained using the noisy ones ($max(I_n)$), for 14 of the experimental records. There is a linear relationship between these two quantities of slope 1.06 and ordinate -0.01. Furthermore, if we associate to each point of the smooth record an error given by the absolute value of the difference with respect to the corresponding value in the noisy record and propagate this error as explained in Appendix 1, we obtain an error, ΔI_s, in the smooth current, I_s, such that the noisy current, I_n, satisfies $I_s - \Delta I_s \leq I_n \leq I_s + \Delta I_s$ at every time. This confirms the conclusions of Fig. 7 showing that the algorithm is stable against noise. We can also observe in Fig. 7, A–B, that relatively rapid temporal changes of the noisy signal translate into brief closing and opening events if we work with the noisy signal, and disappear when working with the smoothed-out one. This is not a particular problem of the algorithm, but is common to analyzing any type of noisy record. A special treatment is needed to distinguish between real opening events and fluctuations when the openings are very brief, and this goes beyond the scope of this article.

DISCUSSION

Summary

We present a novel algorithm that reconstructs, using a minimum number of assumptions, the Ca^{2+} fluxes underlying line-scan fluorescence images of local cytosolic Ca^{2+} transients (e.g., *sparklets* and *puffs*). The algorithm belongs to the backward-calculation class, in which the underlying Ca^{2+} current is inferred from the fluorescent image (Blatter et al., 1997; Rios et al., 1999; Rios and Brum, 2002; Soeller and Cannell, 2002). Most previous implementations of this method explicitly include known binding parameters for cytoplasmic Ca^{2+}, although in some cases
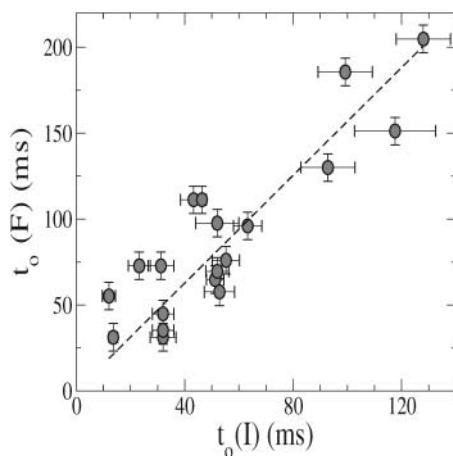
FIGURE 8 Open time obtained from the time series of the fluorescence as a function of the one obtained using the reconstructed current for all the events whose current we could determine using the algorithm. The relationship is approximately linear, with slope 1.58.
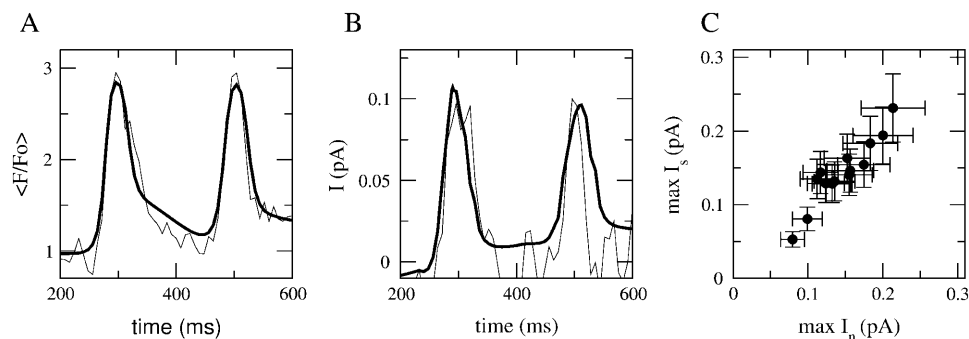
FIGURE 9 Comparison of the application of the algorithm to noisy records obtained by an eight-neighbor averaging of the acquired data and to smoother records obtained with a nonlinear function fitting (see Methods). (*A*) Temporal profiles of the fluorescence for the noisy (*thin lines*) and the smooth (*thick lines*) records. (*B*) Similar to *A*, but for the temporal profiles of the current obtained with the algorithm. (*C*) Maximum value of the current obtained by applying the algorithm to the smooth records, $max(I_s)$, as a function of the maximum values obtained by applying it to the noisy records, $max(I_n)$. We observe a linear relationship of slope 1.06.

(Blatter et al., 1997) certain parameters are adjusted to provide the best agreement with the observations. However, in all cases, a defined model of the intracellular Ca^{2+} dynamics has always been required. The main contribution of our algorithm is the lack of requirement of a detailed explicit model for this dynamics. Thus, it can readily be applied regardless of the cell type. All published studies to date have been applied to estimate the Ca^{2+} release flux associated with Ca^{2+} sparks in muscle—a cell type in which the parameters of Ca^{2+} handling (buffer kinetics, SERCA pumps, etc.) are well characterized. This is not the case for most other cell types. In particular, little is known of the buffers and pumps in *Xenopus* oocytes, which are a favored cell system for study of IP_3-mediated Ca^{2+} signaling (Yao et al., 1995). We were thus motivated to develop an algorithm that requires minimal a priori information, and could therefore be applied to reconstruct the Ca^{2+} flux underlying IP_3-evoked puffs.

The algorithm is based on the hypothesis that the future dynamics of a single variable can be inferred from its previous time evolution, even if this evolution is the result of the interaction with several other variables (Packard et al., 1980; Mindlin et al., 1990, 1998; Gouesbet, 1992). Assuming that the effects of endogenous buffers and sequestration are of relatively short range in space and time, we use Eq. 5 instead of a detailed kinetic model to describe their effects. The functions in this ansatz are determined directly from the experimental images. This is the main new feature of our approach as compared to previous methods (Blatter et al., 1997; Rios et al., 1999; Rios and Brum, 2002; Soeller and Cannell, 2002). We have recently shown that Eq. 5 correctly describes the spatiotemporal dynamics of the Ca^{2+} concentration in the presence of a dye and a pump, even when the dye is slow and an adiabatic approximation does not hold (Ventura et al., 2004). However, as illustrated by some simulations of this article, if Ca^{2+} sequestration occurs very fast upon release and the dye is unable to detect those rapid $[Ca^{2+}]$ changes, the algorithm underestimates the Ca^{2+} current. This problem is mitigated by using some records obtained with a large enough dye

concentration. The algorithm has other assumptions that are common to most methods presented in the literature. We assume that the release occurs in a spatially localized region, that the dye only binds to Ca^{2+} (according to the reaction scheme, Eq. 27; in Soeller and Cannell, 2002, and Smith et al., 1998, the interaction of the dye with other species is also considered), and that the dye and the basal Ca^{2+} are initially uniformly distributed throughout the cytosol. Although the validity of this last assumption is hard to determine in real experiments, the preprocessing described in Methods, above, aims at obtaining the image equivalent to the real one that would have been obtained had the dye and the basal Ca^{2+} been uniformly distributed.

Verification with synthetic data

When tested with synthetic, noise-free data, the algorithm accurately reconstructs the kinetics of the Ca^{2+} source both for stepwise changes in flux that mimic the opening and closing of a single channel (Figs. 3 *A* and 5 *F*) and in determining the relevant timescale of an exponentially decaying flux (Fig. 3, *C* and *D*). Morphological aspects of (spherically symmetric) sources can be determined fairly well too (Fig. 3 *B*). The symmetry requirement is not an inherent limitation of the algorithm but results from the linear-scan method used to obtain the images. The algorithm is also able to identify multiple openings and closings at a site (Figs. 4 and 7).

The precision with which the algorithm predicts the total released current depends on how well the functions g, f, h, and k that define Eq. 5 can be determined from experiment, something that can be done quite accurately, under ideal conditions, if the dye concentration is large enough. But even when the current magnitude is underestimated, the relationship between the actual and the reconstructed current is always linear. Application of the algorithm to (in-focus) numerically generated images obtained with a simple model with fluo-4 dextran, one extra buffer, and a pump provided a linear relationship between the actual and the reconstructed current with a slope that could be very close to 1, depending

on the way we performed the optimization procedure. Namely, we noticed that the values of f, g, and h were relatively small and some of them highly fluctuating in the high $[Ca^{2+}]$ region (Fig. 1 F). By setting these functions equal to zero and determining only k we could obtain cleaner results and current estimates that were 20% better. For this reason, we decided to present only the results obtained in this way in all cases (except for Fig. 1). Taking the simulations of Fig. 2 as a starting point, we observe that the released current estimate gets worse when we work with an image for which the line-scan does not go through the center of release but has a certain offset (Fig. 5 A). The estimate gets better when blurring and offset are included, because light is collected from a finite volume rather than a point (Fig. 5 B). The slope does not decrease too much when only blurring is included, if the (high) spatial resolution of the simulations is kept (Fig. 5 C), but decreases by 30% when only data with the expected resolution of a real experiment is kept ($d \sim 0.15 \mu m$) (Fig. 5 D). This effect can be reverted by applying a deblurring procedure to the blurred data, obtaining a slope that differs by 7.5% with respect to the one obtained with clean high-resolution data. If there is an offset, deblurring the data could give a worse current estimation than applying the algorithm directly to the blurred image (Fig. 5 B). For these reasons, we applied the algorithm to real experimental signals without any previous deblurring. In preanalyzing the $[Ca^{2+}]$ distribution, we can put some bounds on the value of the offset for experimental images in which the Ca^{2+} source is contained within one pixel. Using this type of analysis, images can either be discarded or corrected upon estimating the value of the offset. The problem of offset is inherent to line-scan recordings, an imaging mode that is commonly used because of its fast time evolution. However, other modalities such as total-internal reflection microscopy (Demuro and Parker, 2004) can provide time-resolved two-dimensional images, and we are presently implementing the algorithm for use with such data.

When tested with synthetic data with added noise of realistic amplitude, the algorithm prescribed currents that were accurate in amplitude and relatively accurate in time course (Fig. 5, G and H). It must be pointed out, however, that opening and closing times are affected if the noise amplitude is too large and the current is too small, having consequences on the temporal fidelity of the reconstructed current. This is a problem that is common to the analysis of very noisy time series. A more thorough discussion on how to distinguish true from false release events in these circumstances goes beyond the scope of the current study and will be discussed elsewhere.

The competition between the processes that shape the cytosolic Ca^{2+} dynamics and the interaction with the dye affect the determination of the functions that define Eq. 5. When the dye is unable to sense the fast $[Ca^{2+}]$ changes, the functions are not correctly determined and the released current is underestimated. This problem is mitigated as the dye concentration is increased (Fig. 6). Furthermore, if the

functions that define Eq. 5 are determined for sufficiently large dye concentrations, then they can be used to analyze records that were obtained with smaller amounts of dye giving better estimates of the released current (Fig. 6). Working with larger amounts of dye could limit the set of experiments that may be subsequently analyzed, since the maximum $[Ca^{2+}]$ values for which the ansatz (Eq. 5) is determined might become too small. In the simulations of Fig. 6, however, the maximum current needed to construct the ansatz and the maximum current that could be inferred with a 75% accuracy were not too different (3 pA and 1 pA, respectively). We can address the issue of what a sufficiently large dye concentration is for each cell type by analyzing whether the functions f, g, h, and k change significantly with features from which they should be independent—among them, the dye concentration or the duration of release. To this end, it is not necessary to use very large amounts of dye. It is sufficient to compare the functions obtained with two sufficiently different dye concentrations. If the functions remain approximately the same (something that can be validated using statistical techniques), we can conclude that the amount of dye is enough to capture the full unknown dynamics. If they change significantly, then an analysis of this change (which goes beyond the scope of this article) could be used to estimate the buffering capacity of the cell and to improve the current estimation. A similar analysis could be done in terms of the release duration. In such a case, the experimental records could be grouped in two sets, according to the duration of the release. If the reconstructed functions, f, g, h, and k, are too different for both groups, then we should conclude that the dye is not following the $[Ca^{2+}]$ dynamics correctly and a larger dye concentration should be used to improve the determination of the functions f, g, h, and k. This is the approach we followed in the analysis of the real sparklets. In any case, even in those cases in which the determined functions are only good to describe the slow $[Ca^{2+}]$ dynamics, the relationship between the reconstructed and the actual current is always linear. This remarkable property implies that the ratios of currents underlying different events are correctly predicted by the algorithm under all circumstances and that the calibration to determine the actual current is needed for only one event.

These results indicate that very detailed models involving a large number of usually unknown parameters are unnecessary to reproduce the observed intracellular $[Ca^{2+}]$ dynamics. Although the type of simplified model that we use in this article (in terms of the Eq. 5) is not good to infer the details of the processes that are at work in the cell, it is good to estimate Ca^{2+} currents from fluorescent images, provided that the ansatz (Eq. 5) can be accurately determined. For validating reconstruction methods using numerically simulated images, most backward methods presented in the literature used the same set of equations for the numerical generation of images and for the reconstruction algorithm. Minor differences between both models already affected the estimated current

(Soeller and Cannell, 2002). The effect of varying the parameter values of the model on the release calculation was investigated in Rios et al. (1999). The average current determined over 157 sparks was 16.9 pA for the default set of parameter values; it decreased to 8.05 pA if all buffer concentrations were decreased by one-third, and increased to 26.9 when either the forward reaction rate of dye and Ca^{2+} or the diffusion coefficient of the dye were changed by a factor of 3. This shows the importance of developing an algorithm with the least a priori information. This is the main contribution of our approach. Although it is limited by the time resolution of the experimental records and the amount of dye that is used, there are ways by which these limitations can be overcome. Using sufficiently large amounts of dye is one of them.

Application to real sparklets

Application of the algorithm to experimentally recorded sparklets generated by Ca^{2+} currents through voltage-gated N-type channels provided a good description of both the channel kinetics and of the Ca^{2+} current. Using the raw fluorescence distribution, the mean open time had been estimated as $t_o \approx 28$ ms in Demuro and Parker (2003). Using the algorithm we could infer a value $t_o(I) \approx (17.8 \pm 6.2)$ ms, which compares much better with the value obtained in patch-clamp experiments ($t_o = 11.5$ ms). The mean Ca^{2+} current obtained with the algorithm ($I = (0.139 \pm 0.012)$ pA) and the one that results by applying the correction factor due to blurring and offset (~ 0.2 pA) were also within its estimated upper bound. The single channel current of these channels had only been measured so far using Ba^{2+} as the carrier, because Ca^{2+} currents are undetectable with the patch-clamp technique (Demuro and Parker, 2003; Lee and Elmslie, 1999). Based on these results the Ca^{2+} current was expected to be below the noise threshold of 0.2 pA (Demuro and Parker, 2003). The value obtained by the algorithm is close enough to this upper bound to assume that the dye is able to follow the intracellular $[Ca^{2+}]$ changes quite closely in this case. We have further tested the accuracy of the reconstructed current by forward integration of the dynamic equation (Eq. 4), using the smooth functional form for M (Eq. 5) given by the algorithm (Fig. 7 D) and a simplified version of the reconstructed current (Fig. 7 F), which is limited by the time and space resolution of the experimental record. Although the numerical simulation does not have added noise, the resulting spatiotemporal distribution of the Ca^{2+}-dye complex differs from the one obtained directly from the experimental record by <14% in amplitude and by quantities of the order of the time and space resolution of the experimental records in the time and spatial spread.

CONCLUSIONS

The algorithm we have presented has several points in common with other backward methods (Blatter et al., 1997;

Rios et al., 1999; Rios and Brum, 2002; Soeller and Cannell, 2002), sharing with them some of their limitations. In particular, it requires the computation of space and time derivatives which are limited by the resolution of the images. Furthermore, numerical derivatives introduce errors that tend to amplify the unavoidable noise present in any experimental signal. However, we have tested the performance of the algorithm when applied to numerical simulations with added Gaussian noise, finding that the amplitude of the reconstructed current is not altered. The time course of the current is more affected since opening and closing times get smeared in the presence of high noise, a problem that is shared by all backward methods. We have been working on a tool of analysis that allows the distinction of true from false release events, which we will discuss elsewhere. Regarding the effect of noise, we obtained extra confidence on the results of the algorithm by comparing the Ca^{2+}-bound dye distribution determined from the (noisy) real experiments with that obtained via a noiseless numerical simulation of the effective dynamic equation prescribed by the algorithm. Both distributions differ in time and spatial spread by quantities of the order of the time and space resolution of the experiments and, in amplitude, by <15%. We further checked the robustness of the algorithm against noise by applying a very strong noise reduction to the experimental images finding results that remained close to those obtained using the noisy initial data. An additional problem of our approach is the fact that the time resolution of the acquisition process imposes limitations on the timescales that can be resolved, resulting in an underestimation of the current when the fast processes cannot be followed. This problem is not a peculiarity of our algorithm; it is ubiquitous in all imaging techniques, in that they are limited by the timescales of the dye and its ability to follow changes in the $[Ca^{2+}]$. The main limitation of our algorithm is the ability to obtain an estimate of the ansatz (Eq. 5) that captures the dynamics of the fast unknown processes, something that can be done if the amount of dye is large enough. But even if Eq. 5 is determined using images for which the amount of dye is not large enough, the algorithm is able to determine the spatial spread and temporal behavior of the release quite accurately, giving a linear relationship between reconstructed and actual currents. This implies that it is necessary to determine the factor by which the current is underestimated only for one current value. This could be done by using records with large enough dye concentrations to obtain the functions in Eq. 5. Other possibilities include an analysis of the results obtained using records with two different dye concentrations or different release durations. Other experimental limitations (blurring, finite space resolution, and offset) also lead to results in which the current is underestimated. More work should be done in the direction of calibrating the method (Zou et al., 2004). Another limitation of the algorithm is the fact it requires more than one event to be implemented and events with the highest $[Ca^{2+}]$ cannot be analyzed. However,

working with real experiments we have concluded that it is not necessary that the maximum $[Ca^{2+}]$ values of the various records be too different; therefore, only a small proportion of the records was used for calibration purposes. Also, the algorithm can be easily automated: e.g., complete analysis of a set of 30 events takes <30 min on a Pentium III PC.

Optical Ca^{2+} imaging provides a relatively noninvasive tool to study the kinetics of individual voltage- and ligand-gated ion channel kinetics (Demuro and Parker, 2003; Zou et al., 2004). However, the temporal and spatial resolution of fluorescence images using Ca^{2+} indicator dyes are reduced by factors including Ca^{2+} binding to buffers and the indicator, dye diffusion, and optical blurring. The algorithm we present here substantially improves the precision with which the magnitude, time course, and spatial distribution of the underlying Ca^{2+} can be estimated, and we show that it provides a fairly accurate description of both the kinetics and Ca^{2+} current of N-type voltage-gated Ca^{2+} channels. We think it can be useful for the analysis of local intracellular Ca^{2+} signals in various cell types; in particular, for the analysis of puffs that arise through the concerted opening of unknown numbers of poorly-characterized IP_3 receptors.

APPENDIX 1: MOTIVATION FOR THE CHOICE OF ANSATZ FOR *M*

Eq. 4 describes the dynamics of the Ca^{2+} concentration. However, it cannot be solved by itself. Both R and M depend on other time-dependent variables, whose time evolution is in turn determined by the $[Ca^{2+}]$ distribution. Whereas R depends on the known spatiotemporal distribution of the dye, M depends on those of the other buffers and capture mechanisms that are poorly known. Assuming that the effects of the pumps can be written in terms of the Ca^{2+} concentration only, $G([Ca^{2+}])$, that the reactions with each of these other buffers, B_i, are of the form

$$Ca^{2+} + B_i \underset{k_{off,i}}{\overset{k_{on,i}}{\rightleftharpoons}} CaB_i, \tag{27}$$
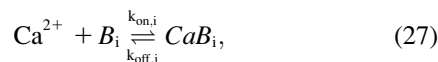
that the free and bound forms of the buffers (B_i, and CaB_i, respectively) diffuse at the same rate, $D_{B,i}$, and that their total concentrations, $[B]_{T,i}$, are uniformly distributed, then

$$M = \sum_i (-k_{on,i}[Ca^{2+}][B_i] + k_{off,i}([B]_{T,i} - [B_i])) + G([Ca^{2+}]), \tag{28}$$

and Eq. 4 has to be solved coupled to equations of the form

$$\frac{\partial [B_i]}{\partial t} = k_{off,i}([B]_{T,i} - [B_i]) - k_{on,i}[Ca^{2+}][B_i] + D_{B,i}\nabla^2[B_i], \tag{29}$$

plus a similar equation for the dye concentration.

Suppose that we know $[Ca^{2+}]$ as a function of space and time (in fact, in the absence of experimental uncertainties, we can obtain it from the fluorescent image if the dye only reacts with Ca^{2+} as done in Step 2 of the algorithm). Then, we can solve each expression in Eq. 29 separately to obtain $[B_i](\mathbf{r}, t)$ (given that we know $[B_i](t = 0)$). So, each value of $[B_i](\mathbf{r}, t)$ is a function of the collection of values, $[Ca^{2+}]$, at all spatial points and previous times, i.e., of $\{[Ca^{2+}](\mathbf{r}', t')$ for all $\mathbf{r}'$ and $t' \le t\}$. It is easy to write

down this dependence explicitly in the cases in which the buffer does not diffuse,

$$[B_i](\mathbf{r}, t) = \exp\left(-k_{off,i}t - k_{on,i}\int_0^t [Ca^{2+}](\mathbf{r}, t')dt'\right)[B_i](\mathbf{r}, 0)$$
$$+ k_{off,i}[B]_{T,i}\int_0^t \exp\left(-k_{off,i}(t - t') - k_{on,i}\right.$$
$$\left. \times \int_{t'}^t [Ca^{2+}](\mathbf{r}, t'')dt''\right)dt', \tag{30}$$

or when Eq. 29 can be linearized, e.g., if $[Ca^{2+}][B_i] \approx [Ca^{2+}][B]_{T,i}$ in Eq. 29,

$$[B_i](\mathbf{r}, t) = [B_i](\mathbf{r}, 0) + [B]_{T,i}$$
$$\times \int d\mathbf{r}' \int_0^t dt' (k_{off,i} - k_{on,i}[Ca^{2+}](\mathbf{r}', t'))e^{-k_{off,i}(t-t')}$$
$$\times \frac{e^{-\frac{(\mathbf{r}-\mathbf{r}')^2}{4D_{B,i}(t-t')}}}{(4\pi D_{B,i}(t - t'))^{3/2}}. \tag{31}$$

The dependence of $[B_i](\mathbf{r}, t)$ with $\{[Ca^{2+}](\mathbf{r}', t')\}$ means that $M(\mathbf{r}, t)$ can also be written in terms of $\{[Ca^{2+}](\mathbf{r}', t')\}$.

Now, the dependence of $[B_i](\mathbf{r}, t)$ on $\{[Ca^{2+}](\mathbf{r}', t')\}$ has a finite memory both in space and time: $[B_i](\mathbf{r}, t)$ depends more strongly on $[Ca^{2+}](\mathbf{r}', t')$ at nearby points, $\mathbf{r}' \approx \mathbf{r}$, and closer times, $t' \approx t$, than at more distant ones. This is so because of the dissipative nature of the evolution equations and the diffusive spatial coupling. It is reflected on the decaying exponentials that appear in Eqs. 30 and 31, which are maximal for $t = t'$ and $\mathbf{r} = \mathbf{r}'$. This finite memory is carried over onto the dependence of M with $\{[Ca^{2+}](\mathbf{r}', t')\}$. If this dependence is only relevant in a small enough neighborhood (both in space and time), then, using a Taylor expansion, we can write all the values $\{[Ca^{2+}](\mathbf{r}', t')\}$ in this neighborhood in terms of $[Ca^{2+}](\mathbf{r}, t)$ and low order derivatives in space and time of Ca^{2+} computed at $(\mathbf{r}, t)$. This is the motivation for choosing the ansatz (Eq. 5), which contains terms with the lowest order derivatives that are compatible with the spherical symmetry of the problem. As discussed in Ventura et al. (2004), an expression for M of Eq. 5 can be obtained analytically under the rapid buffering approximation (Wagner and Keizer, 1994). In that case, the derivation provides analytic expressions for the functions f, g, h, and k.

APPENDIX 2: DESCRIPTION OF HOW THE FUNCTIONS *F*, *G*, *H*, AND *K* AND THEIR ERRORS ARE OBTAINED

Let us call N_i, the number of data points, $\zeta_{j,k}(C_i) \equiv (r_j, t_k)(C_i)$, such that $C_i \le [Ca^{2+}](r_j, t_k)(C_i) < C_{i+1}$. Let us label the data points, $\zeta_{j,k}(C_i)$, by the subscript ℓ (i.e., each ℓ is an integer number associated to each data point, $\zeta_{j,k}(C_i)$; therefore $1 \le \ell \le N_i$, for each C_i). Actually, we should use the notation $\ell(i)$, but we drop the i dependence of ℓ to simplify it. Then, following the notation of Press et al. (1992), we define

$$y_\ell^{(i)} \equiv M(\zeta_{j,k}(C_i)) = \frac{\partial [Ca^{2+}]}{\partial t}\bigg|_{\zeta_{j,k}(C_i)} - R(\zeta_{j,k}(C_i))$$
$$- D_{Ca}\nabla^2[Ca^{2+}]\big|_{\zeta_{j,k}(C_i)}, \tag{32}$$

$$a_1^{(i)} \equiv g_i, \ a_2^{(i)} \equiv f_i, \ a_3^{(i)} \equiv h_i, \ a_4^{(i)} \equiv k_i, \tag{33}$$

$$X_{\ell 1}^{(i)} \equiv \frac{\partial [Ca^{2+}]}{\partial t}\bigg|_{\zeta_{j,k}(C_i)}, \quad X_{\ell 2}^{(i)} \equiv \nabla^2[Ca^{2+}]\big|_{\zeta_{j,k}(C_i)},$$

$$X_{\ell 3}^{(i)} \equiv |\nabla[Ca^{2+}]|^2_{\zeta_{j,k}(C_i)}, \quad X_{\ell 4}^{(i)} = 1. \tag{34}$$

Let us call $\sigma_\ell^{(i)}$ the error of $y_\ell^{(i)}$, which can be computed by error propagation of the right-hand side of Eq. 32. Then, we define the *merit* function for each C_i value as

$$\chi_i^2 = \sum_{\ell=1}^{N_i} \left(\frac{y_\ell^{(i)} - \sum_{n=1}^{4} a_n^{(i)} X_{\ell n}^{(i)}}{\sigma_\ell^{(i)}} \right)^2. \qquad (35)$$

For each binned $[Ca^{2+}]$ concentration value, C_i, the best values of $\{a_n^{(i)}\}_{n=1}^4$ are those that minimize χ_i^2. We perform this minimization by means of a singular value decomposition of the matrix $X_{\ell n}^{(i)}/\sigma_\ell^{(i)}$ (Press et al., 1992). For each $n = 1, \ldots, 4$, we need the set of values, $\{a_n^{(i)}\}_{n=1}^4$, to approximate continuous functions, $\{a_n[Ca^{2+}]\}_{n=1}^4$ (the functions g, f, h, and k). To guarantee continuity, we use the value obtained for $a_n^{(i)}$ as the initial seed to start the minimization procedure that determines $a_n^{(i+1)}$. To determine the errors of the values $\{a_n^{(i)}\}_{n=1}^4$ obtained in this way, we follow Press et al. (1992). Namely, we define the *design* matrix, $\mathbf{A}^{(i)}$, as the $N_i \times 4$ matrix whose elements are given by $A_{\ell m}^{(i)} = X_{\ell m}^{(i)}/\sigma_\ell^{(i)}$. We call $\alpha^{(i)} = (\mathbf{A}^{(i)})^T \cdot \mathbf{A}^{(i)}$, which is a square matrix, and $c^{(i)} = (\alpha^{(i)})^{-1}$, its inverse. Then, the diagonal elements of $c^{(i)}$ are the variances (squared uncertainties) of the fitted parameters, $\{a_n^{(i)}\}$, $1 \le n \le 4$ (Press et al., 1992). Taking the square-root of these variances we obtain the errors, $\{\Delta a_n^{(i)}\}$, $1 \le n \le 4$. Once we have estimates of $\{a_n^{(i)}\}$, $1 \le n \le 4$, for each of the binned $[Ca^{2+}]$ values, C_i, we then have an approximation for the values that the functions f, g, h, and k take on at these binned values (which are $a_2^{(i)}$, $a_1^{(i)}$, $a_3^{(i)}$, and $a_4^{(i)}$, respectively). We then seek continuous functions that can take on these values by fitting the points with a nonlinear curve obtained using a feedforward neural network. We illustrate here the way we estimate the error of this interpolation with the function g, and we proceed similarly with the other functions. For each C_i we define $E_+^{(i)} = |a_1^{(i)} + \Delta a_1^{(i)} - g(C_i)|$ and $E_-^{(i)} = |a_1^{(i)} - \Delta a_1^{(i)} - g(C_i)|$, where g is the smooth $[Ca^{2+}]$-dependent function that we obtained by fitting the discrete set of points, g_i. Then, for $[Ca^{2+}] \in (C_i, C_{i+1})$ we define $\Delta g([Ca^{2+}]) \equiv \max\{E_+, E_-\}$.

The term M that we are trying to determine with this optimization procedure is mainly given by the reactions with buffers other than the dye (see Appendix 1). Thus, we expect that a similar ansatz (but with different functions f_R, g_R, h_R, and k_R) will hold for R, the term due to the reaction with the dye defined in Eq. 3. Therefore, inserting the ansatz for R in Eq. 4 we see that there is a trivial solution for the ansatz of M: $g = 1 - g_R f = -D_{Ca} - f_R$, $h = -h_R$, and $k = -k_R$. This is not the ansatz we are after since it only holds in regions with $Q_{Ca} = 0$. Thus, there is not a unique solution for our optimization procedure, and this introduces some difficulties. To study this problem, we minimized χ_i^2 in Eq. 35, using different tolerances, yet always obtaining similar results. However, as displayed in Fig. 1 F, we observed that f, g, and h were relatively small, and that f and g were highly fluctuating for large $[Ca^{2+}]$ values, as if the optimization procedure was converging to different minima for slightly different $[Ca^{2+}]$ values. Furthermore, the magnitudes of the first three terms ($g(\partial[Ca^{2+}]/,)f\nabla^2[Ca^{2+}]$ and $h|\nabla[Ca^{2+}]|^2$) in Eq. 5 are $\le 20\%$ of the magnitude of k. For this reason, we decided to minimize χ_i^2, setting $f = g = h = 0$ and only determining k. We obtained cleaner results and better current estimates and these are the results that we show in this article (except for Fig. 1). The ability to fit M by using only a function of $[Ca^{2+}]$ is related to the mathematical properties of the *solutions* of the dynamic equations in the presence of localized currents, but not of the dynamic equations in general. We will discuss the mathematical properties of these solutions with further detail in another article.

REFERENCES

Allbritton, N. L., T. Meyer, and L. Stryer. 1992. Range of messenger action of calcium ion and inositol 1,4,5-triphosphate. *Science*. 258:1812–1815.

Baylor, S. M., S. Hollingworth, and W. K. Chandler. 2002. Comparison of simulated and measured calcium sparks in intact skeletal muscle fibers of the frog. *J. Gen. Physiol*. 120:349–368.

Blatter, L. A., J. Hüser, and E. Ríos. 1997. Sarcoplasmic reticulum Ca^{2+} release flux underlying Ca^{2+} sparks in cardiac muscle. *Proc. Natl. Acad. Sci. USA*. 94:4176–4181.

Cheng, H., W. J. Lederer, and M. B. Cannell. 1993. Calcium sparks: elementary events underlying excitation-contraction coupling in heart muscle. *Science*. 262:740–744.

Demuro, A., and I. Parker. 2003. Optical single-channel recording: imaging Ca^{2+} flux through individual N-type voltage-gated channels expressed in *Xenopus oocytes. Cell Calcium*. 34:499–509.

Demuro, A., and I. Parker. 2004. Imaging the activity and localization of single voltage-gated Ca^{2+} channels by total internal reflection fluorescence microscopy. *Biophys. J*. 86:3250–3259.

Izu, L. T., J. R. Mauban, D. W. Balke, and W. G. Wier. 2001. Large currents generate cardiac Ca^{2+} sparks. *Biophys. J*. 80:88–102.

Gouesbet, G. 1992. Reconstruction of vector fields: the case of the Lorenz system. *Phys. Rev. A*. 46:1784–1796.

Hille, B. 2001. Ion Channels of Excitable Membranes. Sinauer Associates, New York.

Lee, H. K., and K. S. Elmslie. 1999. Gating of single N-type calcium channels recorded from bullfrog sympathetic neurons. *J. Gen. Physiol*. 113:111–124.

Lin, Z., S. Haus, J. Edgerton, and D. Lipscombe. 1997. Identification of functionally distinct isoforms of the N-type Ca^{2+} channel in rat sympathetic ganglia. *Neuron*. 18:153–166.

Lukyanenko, V., T. F. Wiesner, and S. Gyorke. 1998. Termination of Ca^{2+} release during Ca^{2+} sparks in rat ventricular myocytes. *J. Physiol*. 507:667–677.

Mindlin, G. B., X. Hou, H. G. Solari, R. Gilmore, and N. B. Tufillaro. 1990. Classification of strange attractors by integers. *Phys. Rev. Lett*. 64:2350–2353.

Mindlin, G. B., N. Merener, and P. T. Boyd. 1998. Low-dimensional dynamics outside the laboratory: the case of roAp stars. *Europhys. Lett*. 42:31–36.

Packard, N. H., J. P. Crutchfield, J. D. Farmer, and R. S. Shaw. 1980. Geometry from a time series. *Phys. Rev. Lett*. 45:712–716.

Press, W. H., S. A. Teukolsky, W. T. Vetterling, and B. P. Flannery. 1992. Numerical Recipes in C. Cambridge University Press, Cambridge, UK. 671.

Pawley, J. B. Editor. 1995. Handbook of Biological Confocal Microscopy. Plenum Press, New York.

Ríos, E., M. D. Stern, A. González, and G. Pizarro. 1999. Calcium release flux underlying Ca^{2+} sparks of frog skeletal muscle. *J. Gen. Physiol*. 114:31–48.

Ríos, E., and G. Brum. 2002. Ca^{2+} release flux underlying Ca^{2+} transients and Ca^{2+} sparks in skeletal muscle. *Frontiers Biosci*. 7:d1195–1211.

Smith, G. D., J. E. Keizer, M. D. Stern, W. J. Lederer, and H. Cheng. 1998. A simple numerical model of calcium spark formation and detection in cardiac myocytes. *Biophys. J*. 75:15–32.

Soeller, C., and M. B. Cannell. 2002. Estimation of the sarcoplasmic reticulum Ca^{2+} release flux underlying Ca^{2+} sparks. *Biophys. J*. 82:2396–2414.

Sun, X.-P., N. Callamaras, J. S. Marchant, and I. Parker. 1998. A continuum of InsP$_3$-mediated elementary Ca^{2+} signaling events in *Xenopus* oocytes. *J. Physiol.* 509:67–80.

Timmer, J., T. Müller, and W. Melzer. 1998. Numerical methods to determine calcium release flux from calcium transients in muscle cells. *Biophys. J.* 74:1694–1707.

Ventura, A. C., L. Bruno, and S. Ponce Dawson. 2004. Probing a reduced equation for intracellular calcium dynamics. *Physica A (Amsterdam)*. 342:281–287.

Wagner, J., and J. Keizer. 1994. Effects of rapid buffers on Ca^{2+} diffusion and Ca^{2+} oscillations. *Biophys. J.* 67:447–456.

Yao, Y., J. Choi, and I. Parker. 1995. Quantal puffs of intracellular Ca^{2+} evoked by inositol trisphosphate in *Xenopus* oocytes. *J. Physiol.* 482: 533–553.

Zou, H., L. M. Lifshitz, R. A. Tuft, K. E. Fogarty, and J. J. Singer. 2004. Imaging calcium entering the cytosol through a single opening of plasma membrane ion channels: SCCaFTs—fundamental calcium events. *Cell Calcium*. 35:523–533.